ACS NANO

www.acsnano.org

ARTICLE

Potassium-Doped MnO_2 Nanoparticles Reprogram Neutrophil Calcium Signaling to Accelerate Healing of Methicillin-Resistant *Staphylococcus aureus*-Infected Diabetic Wounds

Jianxu Wei,[#] Xiaomeng Zhang,[#] Baiyan Sui,[#] Xinxin Ding, Yuan Li, Beilei Liu, Jiale Wang, Xiaolei Lv, Yi Zhang, Xue Jiang, Yijie Yang, Hongchang Lai,* Xin Liu,* and Junyu Shi*

Cite This: *ACS Nano* 2025, 19, 11807−11822

Read Online

ACCESS | Metrics & More | Article Recommendations | Supporting Information

ABSTRACT: Neutrophils, as first-line immune cells, typically lose their edge within the diabetic wounds accompanied by methicillin-resistant *Staphylococcus aureus* (MRSA) infections (the D/M setting), playing the role of "more foe than friend" during the healing process. Specifically, reduced influx of calcium ions (Ca^{2+}) and impaired calcium homeostasis yield the dysfunction of neutrophil sequential behaviors in pathogen killing and wound healing, manifesting as suppressed chemotaxis, decreased intracellular reactive oxygen species (ROS) generation, prolonged apoptosis, and retention of neutrophil extracellular traps (NETs). To address this challenge, this study fabricated potassium (K)-doped manganese dioxide nanoparticles (MnO_2 NPs), which activated transmembrane Ca^{2+} channels by inducing neutrophil depolarization via electron transfer. Subsequently, this contributed to the initial Ca^{2+} influx and reprogrammed Ca^{2+}-dependent behaviors of impaired neutrophils. Also, the potential antimicrobial capacity of K-MnO_2 NPs created a favorable extracellular environment that restored calcium homeostasis, enabling apoptotic neutrophils to be removed timely. Therefore, the wounds treated with K-MnO_2 NPs in the D/M setting exhibited potent resistance to MRSA and rapid healing, which could be attributed to the synergistic effects of K-MnO_2 NPs in leveraging Ca^{2+} influx and maintaining calcium homeostasis. In brief, K-MnO_2 NPs constitute an effective strategy to resist MRSA and rapid wound healing in the D/M setting.

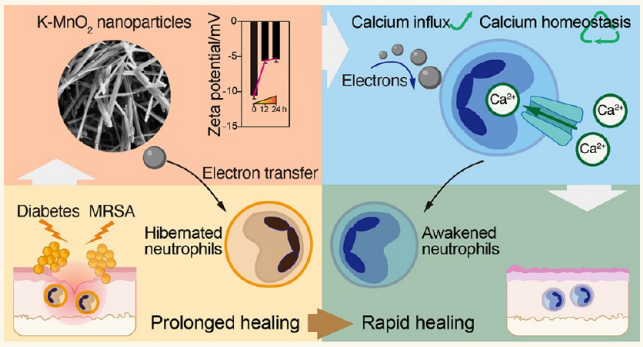

KEYWORDS: *neutrophils, electron transfer, calcium, diabetic wounds, MRSA*

1. INTRODUCTION

Because of chronic inflammation, repeated infection, and drug resistance, diabetic wounds colonized with MRSA have become a major concern. Traditional strategies like wound dressings and NPs are commonly used to treat diabetic wounds. However, they have limited bactericidal effects and single functions, and are unable to activate the repair potential by regulating autoimmunity,[1−3] resulting in a suboptimal healing outcome.

Neutrophils, as first-line immune cells that swarm to the damaged site, are crucial for early infection control and initiating the wound healing process.[4] However, the confluence of the D/M setting gives rise to the dysfunction in neutrophil functional homeostasis, fundamentally reversing their role (neutrophils from friend to foe) in wound healing. Neutrophil "beneficial" behaviors in response to infection, such as recruitment, phagocytosis, and intracellular ROS production, are generally impaired.[5] Meanwhile, their "deleterious" behaviors, particularly the prolonged efferocytosis of apoptotic neutrophils and

Received: October 6, 2024
Revised: March 8, 2025
Accepted: March 10, 2025
Published: March 18, 2025

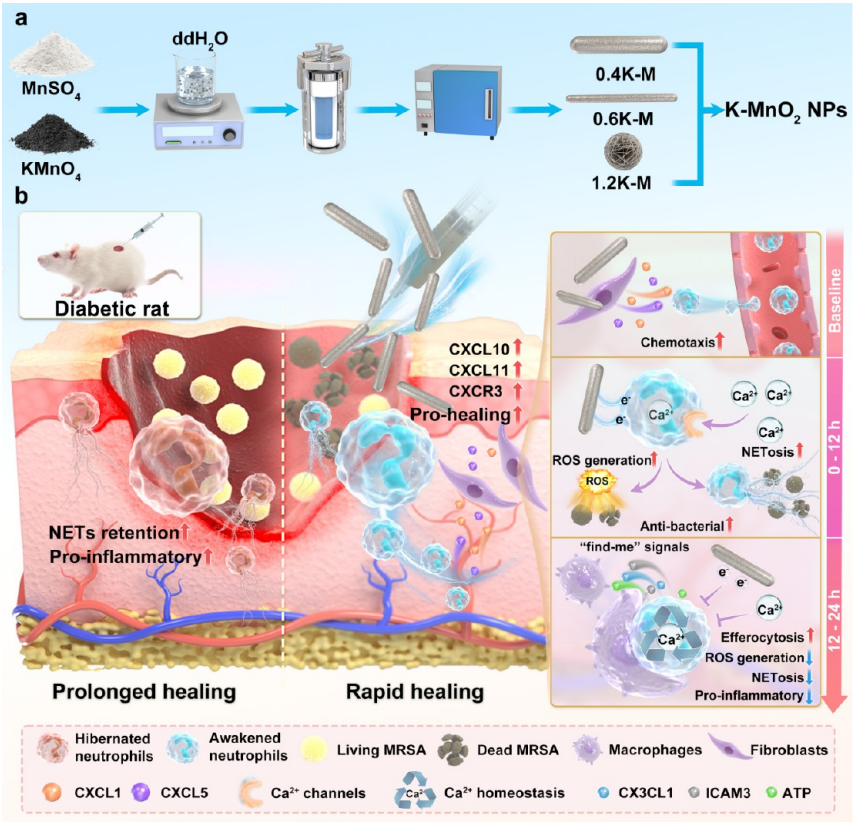

Figure 1. Schematic diagram of a) the formation of K-MnO_2 NPs, and b) their effects on reprograming calcium signaling to enhance neutrophil functions in the healing process of MRSA-infected wounds.

retention of NETs, are dramatically activated. The interplay between these two adverse dysfunctions ultimately contributes to aberrant inflammation and uncontrolled infection, severely impeding the repair process in the D/M setting.[6,7] Therefore, existing therapies more often consider damaged neutrophils as harmful factors.[7] Previous drugs and biomaterials, like hyaluronic acid[8,9] and dexamethasone-loaded hydrogels,[10,11] were employed to block neutrophil recruitment, disarm localized neutrophils, and expel them from affected areas. Nevertheless, a large proportion of neutrophils simply enter a hibernation-like state in the D/M setting,[12] and their potential for bacterial resistance and tissue repair has not been lost but is only temporarily suppressed. It is truly regrettable that these remedies overlook the hidden benefits of neutrophils. Even vancomycin (Van), the gold standard for treating MRSA infections, has been found to impair rather than harness neutrophils' favorable behaviors.[13] It remains elusive how to awaken hibernating neutrophils and effectively reprogram their behaviors.

Ca^{2+} plays a pivotal role in regulating various neutrophil behaviors, potentially serving as a wake-up call for hibernating neutrophils,[14−16] As reported, diabetes combined with microbial infections leads to decreased intracellular Ca^{2+} levels and impaired calcium homeostasis in neutrophils. Under pathological hyperglycemia, highly active MRSA readily infiltrates neutrophils, significantly inhibiting the activation of initial Ca^{2+} influx. This results in the irresponsiveness of neutrophil recruitment, phagocytosis, and intracellular ROS generation. More seriously, merely stimulating Ca^{2+} influx is still inadequate. Dysfunctional calcium homeostasis exacerbates Ca^{2+} overload, thereby delaying the "find-me" signals for efferocytosis and prolonging the retention of NETs, which is detrimental to tissue repair.[17,18] Therefore, a comprehensive approach capable of activating initial Ca^{2+} influx and restoring calcium homeostasis to a healthy state is required. Such a strategy not only reactivates hibernating neutrophils and impedes MRSA infiltration into neutrophils, but also creates an environment conducive to maintaining calcium homeostasis and thus timely expulsion of apoptotic neutrophils from localized tissues. This can be considered a "smart" strategy to facilitate wound healing in the D/M setting.

Activation of transmembrane voltage-gated Ca^{2+} channels (VGCCs), an essential prerequisite for stimulating Ca^{2+} influx, is closely related to changes in cell membrane potential. Recent studies have demonstrated that extracellular electrons supplied by metal semiconductors can modulate membrane potential and activate VGCCs.[19,20] Considering this, this study introduced nanoscale MnO_2 semiconductors that not only possess reliable antimicrobial properties but also outperform other metal oxides such as ZnO, CuO, Fe_3O_4, and Al_2O_3.[21] Furthermore, potassium ions (K^+) were incorporated to enhance the electron mobility of MnO_2 NPs.[22,23] Herein, extracellular electrons released from K-MnO_2 NPs attempt to alter the membrane potential of damaged neutrophils and activate downstream Ca^{2+} signaling,[19] thereby awakening the hibernating neutrophils. Additionally, incorporating K^+ enhances the NPs' antimicrobial activity against MRSA,[23] fostering a more sterile environment for neutrophils, which is essential for maintaining calcium homeostasis. Overall, this study proposes a nonantibiotic approach, namely K-MnO_2 NPs, to attenuate inflammation, combat MRSA infection, and promote diabetic wound healing. By leveraging Ca^{2+} signaling through electron transfer, we endeavor to timely reprogram the

https://doi.org/10.1021/acsnano.4c14057
ACS Nano 2025, 19, 11807−11822

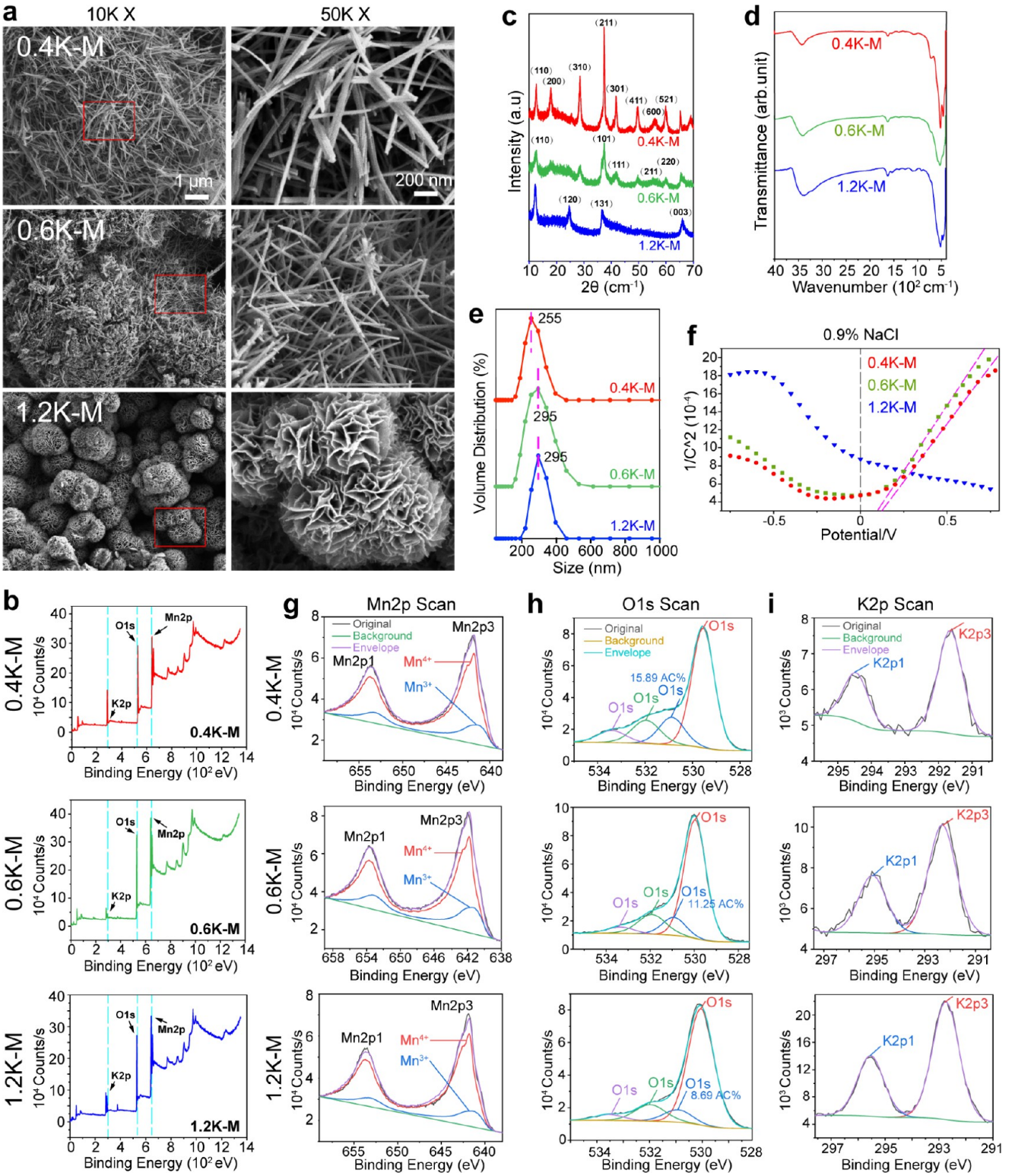

Figure 2. Characteristics of K-MnO_2 NPs. a) K-MnO_2 NPs morphologies detected by SEM at magnifications of 10K (scale bar: 1 μm) and 50K (scale bar: 200 nm), respectively. b) Elemental composition of K-MnO_2 NPs measured by XPS spectra. c) XRD patterns and d) FT-IR spectra detection of K-MnO_2 NPs. e) Particle size of K-MnO_2 NPs measured by DLS. f) Semiconductive types of K-MnO_2 NPs determined by M-S curves. g-i) Curve fitting analysis of characteristic elements including Mn, O, and K, with atomic concentration percentages (AC%) provided.

dysfunctional behaviors of damaged neutrophils, enabling these cells to play a role of "more friend than foe" in the context of diabetic wound healing.

2. RESULTS

2.1. Characteristics of K-MnO_2 NPs. Based on the varying K doping levels, the different groups of K-MnO_2 were designated as 0.4K-M, 0.6K-M, and 1.2K-M, respectively. In the study, the pilot cytotoxicity screening identified that 100 μg

https://doi.org/10.1021/acsnano.4c14057
ACS Nano 2025, 19, 11807−11822

mL^{-1} of K-MnO_2 NPs optimally promoted fibroblast viability (Figure S1a). Thus, this concentration was selected for further investigations. SEM analysis revealed distinct morphologies for different K-MnO_2 NPs (Figure 2a). Specifically, 0.4K-M appeared as rods, 0.6K-M as fibers, and 1.2K-M as flower-like structures at 50K magnification. XPS results confirmed the presence of characteristic elements including K, O, and Mn (Figure 2b). Notably, only K 2p3 (290−294 eV) was detected in the K core-level (Figure 2i), indicating complete filling of K ions.[22] XRD analysis indicated that the spacing between the diffraction peaks widened with the increased K^+ content (Figure 2c). Specifically, the diffraction characteristic peaks of 0.4K-M were 12.6°, 17.9°, 28.5°, 37.4°, 41.8°, 49.6°, 56.5°, and 60.0°, respectively, indicating (110), (200), (310), (211), (301), (411), (600), and (521) crystal planes of α-MnO_2 (JCPDS card No.: 44−0141); The diffraction characteristic peaks of 0.6K-M were 28.7°, 37.4°, 42.0°, 56.9°, and 60.02°, respectively, representing (110), (101), (111), (211), and (220) crystal planes of β-MnO_2 (JCPDS card No.: 024−0735). The diffraction characteristic peaks of 1.2K-M were 24.6°, 36.6°, 37.0°, and 66.0°, respectively, representing (120), (031), (131), and (003) crystal planes of δ-MnO_2 (JCPDS card No.: 14−0644). FT-IR results revealed several absorption bands at wavelengths of 3300−3600, 1500−1800, 900−1200, and 400−600 cm^{-1} (Figure 2d). The bands in the range of 3300−3600 cm^{-1} originated from the O−H stretching vibration, and the O−H bending vibration in the range of 1000−1800 cm^{-1} was attributed to Mn atoms. The absorption bands in the range of 400−900 cm^{-1} were attributed to the Mn−O vibrations.[24] The consistency between FT-IR and XRD results confirmed this study's successful preparation of different K-MnO_2 NPs. The results of DLS revealed that K-MnO_2 NPs exhibited good stability, with the particle size of 0.4K-M centered at approximately 255 nm, while those of 0.6K-M and 1.2K-M centered at roughly 295 nm (Figure 2e). The sedimentation experiments revealed that K doping significantly enhanced the sedimentation rate of all K-MnO_2 NPs, leading to their complete sedimentation within approximately 30 min (Figure S2c). Such a property is beneficial as it allows the NPs to rapidly maintain a stable local concentration and exert their effect. Meanwhile, the reduced dispersion makes it less likely for the NPs to enter the blood circulation, minimizing its systemic impact and thus conforming better to biosafety requirements.

The binding energy (BE) of each element is displayed in Table 1. The bandgaps of Mn 2p increased by 0.2 and 0.55 eV in 0.6K-M and 1.2K-M, respectively, suggesting a decrease in the number of transferred electrons in 0.6K-M and 1.2K-M.[25,26] Also, the bandgaps of K-MnO_2 NPs increased with the incorporation of more K ions (Figure S2a), indicating that the addition of 0.4 g K^+ may enhance the conductivity of MnO_2 NPs, and the conductivity of 0.6K-M seemed to surpass that of 1.2K-M. Based on the Mott−Schottky (M-S) curves depicted in Figure 2f, both 0.4K-M and 0.6K-M were identified as N-type semiconductors, while 1.2K-M was identified as a P-type semiconductor. The slope values of the M-S curves suggested that 0.4K-M possessed a higher electron density and a greater potential for electron transfer than 0.6K-M (Figure S2a).

Table 1. XPS Element Binding Energy (eV) of Each Element of K-MnO_2 NPs

	K 2p	O 1s	Mn 2p
0.4K-M	291.05	528.97	641.44
0.6K-M	291.43	529.20	641.64
1.2K-M	292.15	529.50	641.99

In Figure 2h, the O 1s XPS spectra were deconvoluted into four peaks, with the peak at 530.9 eV attributed to the oxygen vacancy.[27] The concentration percentages of each group were presented in descending order: 0.4K-M (15.89%) > 0.6K-M (11.25%) > 1.2K-M (8.69%). The ion release profiles of K-MnO_2 NPs showed that within 28 days, 1.2K-M exhibited the highest K ion release level and the lowest Mn ion release level among all groups ($p < 0.001$). Conversely, 0.4K-M showed the lowest K ion release level and a moderate Mn ion release level (Figure S2b).

2.2. RNA Sequencing for Detecting K-MnO_2 NPs Effects on Impaired Neutrophils in the D/M Setting. Initially, our study intended to explore the lifespan of neutrophils in the D/M setting, which was crucial for understanding the interaction pattern between K-MnO_2 and neutrophils. Previous studies have mentioned that the lifespan of neutrophils *in vitro* is approximately 24 h,[28] but the specific lifespan in the D/M setting remains unknown. Our findings revealed that within the first 12 h, most neutrophils (over 60%) remained active and healthy. However, after 24-h incubation, most cells (around 80%) began to enter the apoptotic phase, suggesting that a substantial number of neutrophils was rapidly compromised within the 12-to-24 h period. Furthermore, within the 24-to-48 h period, nearly all cells underwent death (Figure S3b−d). Therefore, the initial 24 h might be a critical phase during which K-MnO_2 exerted a pivotal influence on neutrophils, and this period will also serve as the key observation window for our subsequent research.

It has been reported that multiple calcium-dependent behaviors of neutrophils against MRSA reach their peak at 12 h.[29] Consequently, RNA sequencing was employed to characterize the genes significantly differentially expressed in neutrophils at this time. Gene Ontology (GO) enrichment analysis results revealed that under the D/M setting, various functional pathways related to neutrophils were highlighted (Figure 3a).

More specifically, the results of Blk vs Ctrl revealed that the D/M setting dramatically suppressed the expression of calcium-related genes (Figure 3b). Meanwhile, it exerted a pronounced inhibitory effect on neutrophil depolarization as well as Ca^{2+} influx (Figure 4a,b). In contrast, K-MnO_2 NPs broadly stimulated diverse types of calcium channel-related genes at 12 h. These encompassed T-type VGCC (*S100a4*, *Camk2d*), L-type VGCC (*Cabp1*, *S100a4*, *Cacnb1*), N-type VGCC (*Calhm2*, *Kcnn3*), and store-operated calcium channels (SOCs; *Cracr2a*). Notably, as compared to the Ctrl group, 0.4K-M led to a low-to-high shift in both cellular depolarization and Ca^{2+} influx within 12 h. However, the other groups displayed no significant activation compared to the Ctrl group. Conversely, when compared with the 0−12 h interval, 0.4K-M did not further aggravate depolarization, and instead, the Ca^{2+} influx underwent a high-to-low shift within 12−24 h. However, within this same period, both 0.6K-M and 1.2K-M exhibited a substantial increase in depolarization and Ca^{2+} influx. Moreover, in Van group, no significant changes were observed regarding depolarization and Ca^{2+} influx.

Furthermore, the study selectively inhibited each type of calcium channel (Figure 4c,d). The result indicated that the D/M setting greatly inhibited Ca^{2+} influx throughout the 24-h period. Interestingly, considering the entire 24 h period for modulating Ca^{2+} influx, 0.4K-M induced a low-to-high shift

https://doi.org/10.1021/acsnano.4c14057
ACS Nano 2025, 19, 11807−11822

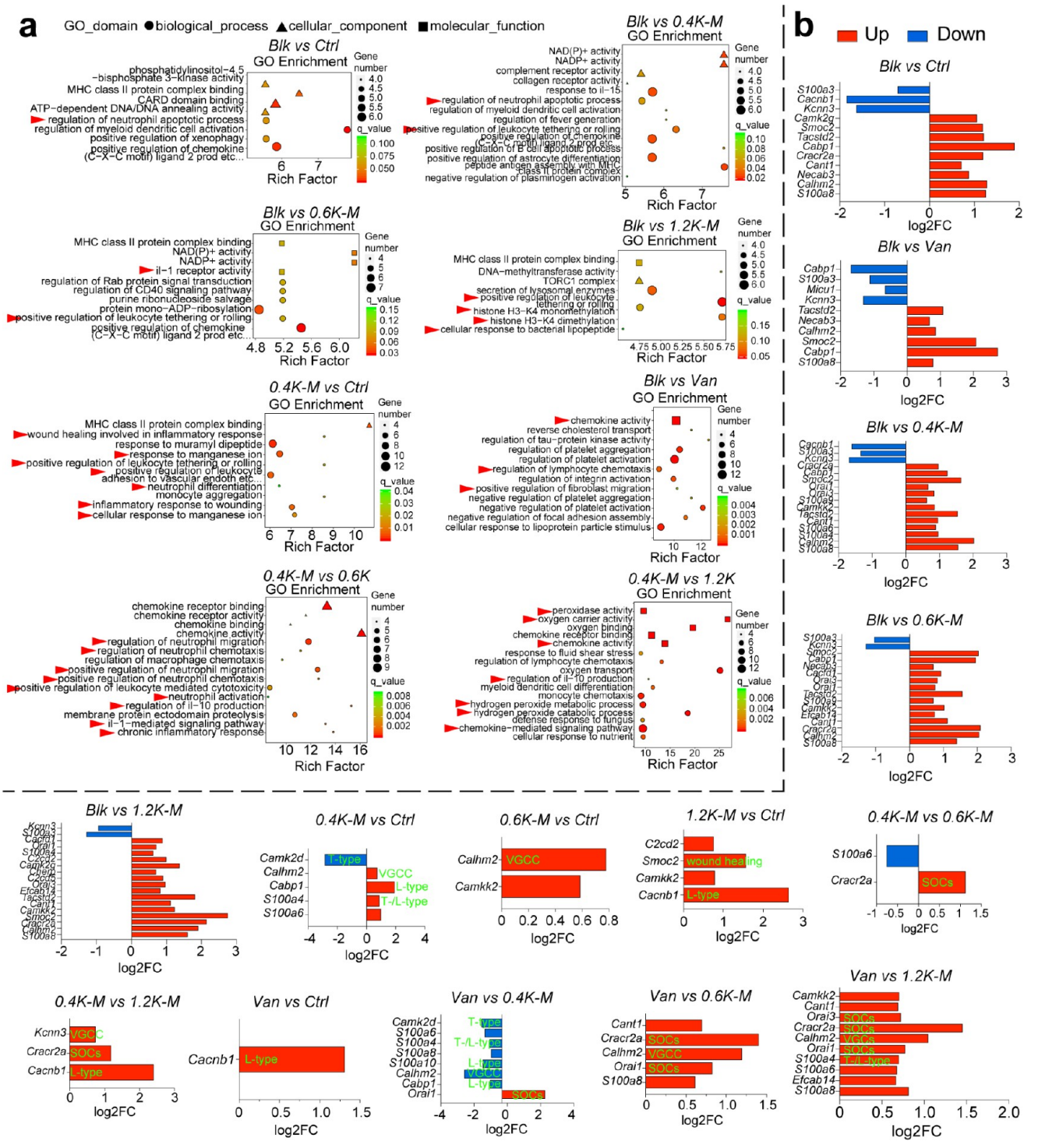

Figure 3. RNA sequencing for detecting K-MnO_2 NPs effects on impaired neutrophils in the D/M setting. a) After 12 h of incubation in the D/M setting, GO enrichment analyses unveil various pathways expressed in impaired neutrophils. Noteworthy pathways associated with calcium ions are highlighted with red arrows. b) Significantly differentially expressed genes regarding various Ca^{2+} channels, including voltage-gated Ca^{2+} channels (VGCC), T-type Ca^{2+} transport channels (T-type), L-type Ca^{2+} transport channels (L-type), and store-operated Ca^{2+} channels (SOCs).

within 0−12h, and a high-to-low shift within 12−24 h. This reprogramming ability to modulate Ca^{2+} influx in a low-to-high-to-low shift over time was not observed in other groups. Moreover, it seemed that only inhibiting the N-type voltage-gated calcium channels could significantly impact the special ability of 0.4K-M to reprogram Ca^{2+} influx (Figure 4c,d).

2.3. K-MnO_2 NPs Activate Neutrophil Depolarization and Ca^{2+} Influx via Electron Transfer in the D/M Setting.

The electron transfer from semiconductive K-MnO_2 NPs to neutrophils serves as a pivotal prelude to the activation of neutrophil depolarization and Ca^{2+} influx (Figure 4e). Thus, this study introduced MnO_2 NP, a typical insulator,[30] as a negative control to compare its differences with the modified semi-

https://doi.org/10.1021/acsnano.4c14057
ACS Nano 2025, 19, 11807−11822

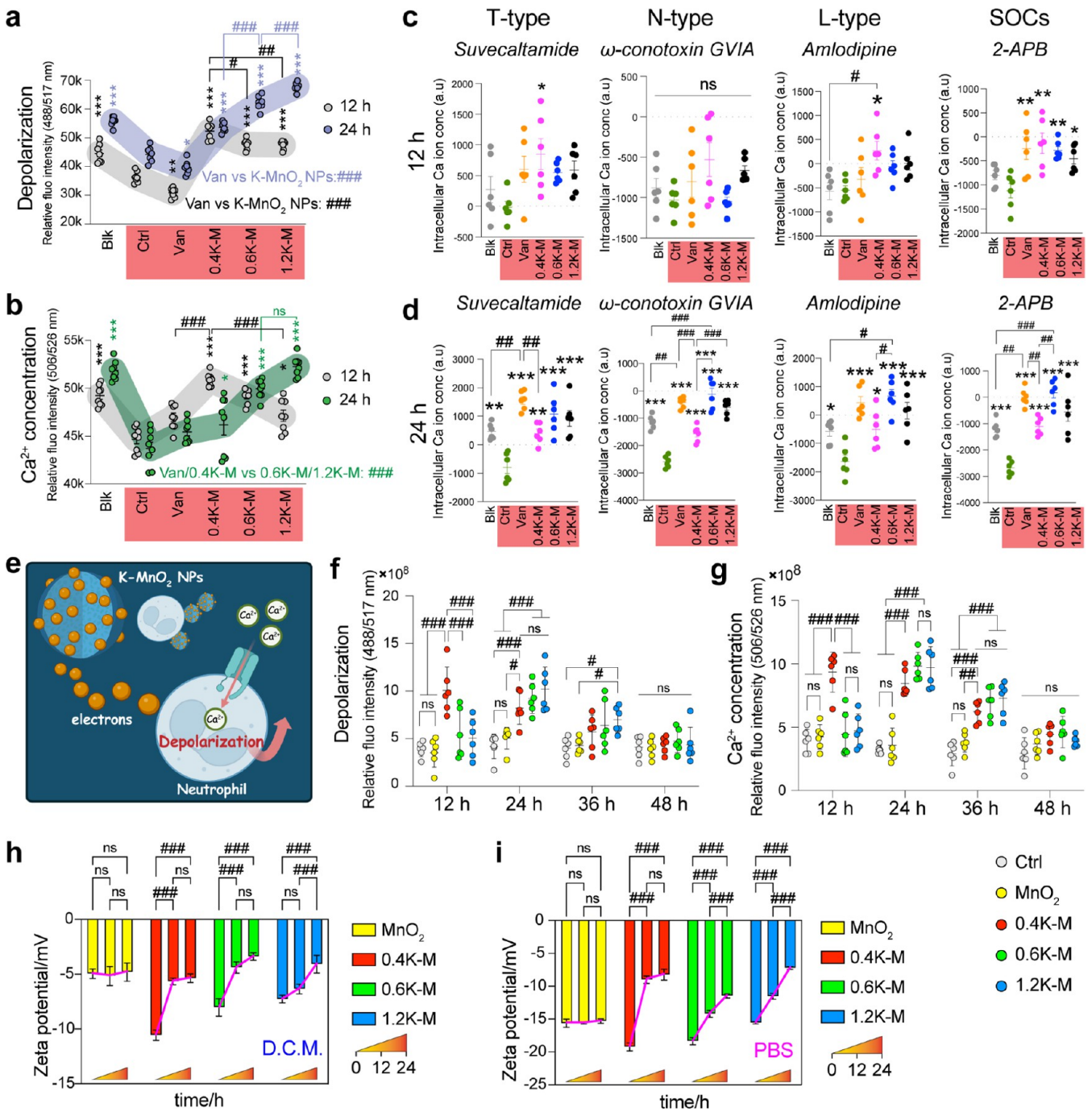

Figure 4. K-MnO_2 NPs activate neutrophil depolarization and Ca^{2+} influx via electron transfer in the D/M setting. a) Neutrophil depolarization and b) intracellular Ca^{2+} concentration in neutrophils are depicted at 12 and 24 h after exposure to K-MnO_2 NPs in the D/M setting. c, d) Following selective inhibition of each Ca^{2+} channel, intracellular Ca^{2+} concentrations are measured at 12, 24 h, respectively. e-i) Verification of electron transfer between K-MnO_2 NPs and neutrophils: e) Diagram depicts electron transfer between K-MnO_2 NPs and neutrophils, and thus activating neutrophil depolarization and initial Ca^{2+} influx (created in BioRender. https://BioRender.com/r97-i002). f) Neutrophil depolarization and g) intracellular Ca^{2+} concentration in neutrophils are depicted from 0 to 48 h after exposure to MnO_2/K-MnO_2 NPs in the D/M setting. h, i) The zeta potential of MnO_2/K-MnO_2 NPs after 0−24 h of coculturing. In the measurement process, D.C.M and PBS were employed as dispersants. The red-colored frames present the D/M culture setting. Abbreviation: Voltage-gated Ca^{2+} channel, VGCC; T-type Ca^{2+} transport channels, T-type; N-type Ca^{2+} transport channels, N-type; L-type Ca^{2+} transport channels, L-type; Store-operated Ca^{2+} channels, SOCs; diabetic conditioned medium, D.C.M. *$p < 0.05$; **$p < 0.01$; ***$p < 0.001$ as compared to Ctrl. $^{\#}p < 0.05$; $^{\#\#}p < 0.01$; $^{\#\#\#}p < 0.001$.

conductive K-MnO_2. In Figure 4h,i, the zeta potential of MnO_2 remained unchanged over 24 h, indicating no electron transfer occurred in MnO_2. After 48 h of coculturing with MnO_2 in the D/M setting, neutrophils exhibited no change in depolarization and Ca^{2+} influx (Figure 4f,g), consistent with the behavior of hibernating neutrophils in the Ctrl group.

In contrast, the zeta potential of different K-MnO_2 NPs decreased over time, suggesting continuous electron loss. Specifically, 0.4K-M carried the highest number of electrons

https://doi.org/10.1021/acsnano.4c14057
ACS Nano 2025, 19, 11807−11822

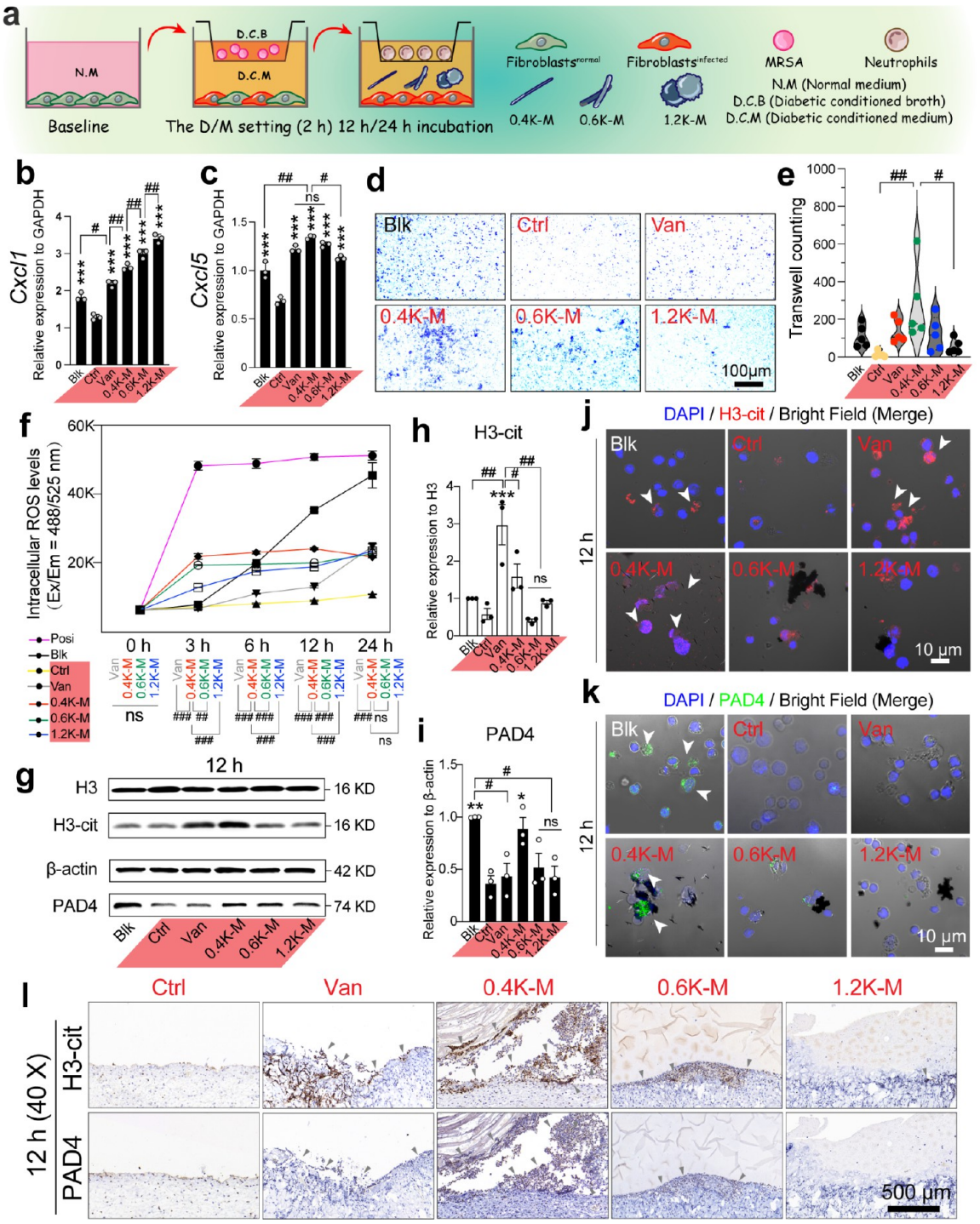

Figure 5. K-MnO_2 NPs reprogram neutrophil sequential behaviors mediated by the activation of initial Ca^{2+} influx in the D/M setting. a) A diagram depicts the establishment of a coculture model in the D/M setting. b, c) Neutrophil chemotaxis-related genes (*Cxcl1*, *Cxcl5*) expressed by fibroblasts in the D/M setting. d) Images of recruited neutrophils at 12 h (scale bar: 100 μm) and e) relevant statistical analysis. f) Intracellular ROS levels in neutrophils within 24 h in the D/M setting. g) WB images of H3-cit and PAD4 expressions at 12 h in the D/M setting, with h, i) relevant statistical analyses. j, k) IF/ICC images of H3-cit and PAD4 expressions in the D/M setting at 12 h *in vitro* (scale bar: 10 μm). l) IHC staining images of H3-cit and PAD4 expressions in the D/M setting at 12 h *in vivo* (scale bar: 500 μm). The red-colored frames represent the D/M culture setting. *$p < 0.05$, **$p < 0.01$, ***$p < 0.001$ as compared to Ctrl; $^{\#}p < 0.05$, $^{\#\#}p < 0.01$, $^{\#\#\#}p < 0.001$.

(the lowest potential) compared to other semiconductors at baseline. Twelve hours later, significant electron release from 0.4K-M into the external region was observed ($p < 0.001$). In response, neutrophils underwent intense depolarization through rapid electron acceptance, accompanied by a substantial influx of Ca^{2+}. Conversely, due to the weaker electron transfer capabilities of 0.6K-M and 1.2K-M, neutrophils failed to be rapidly activated after the first 12 h of interaction. However, through sustained electron transfer, these neutrophils were eventually activated at 24 h. Unfortunately, since the lifespan of most neutrophils does not exceed 24 h (Figure S3b–d), the activation state of

https://doi.org/10.1021/acsnano.4c14057
ACS Nano 2025, 19, 11807–11822

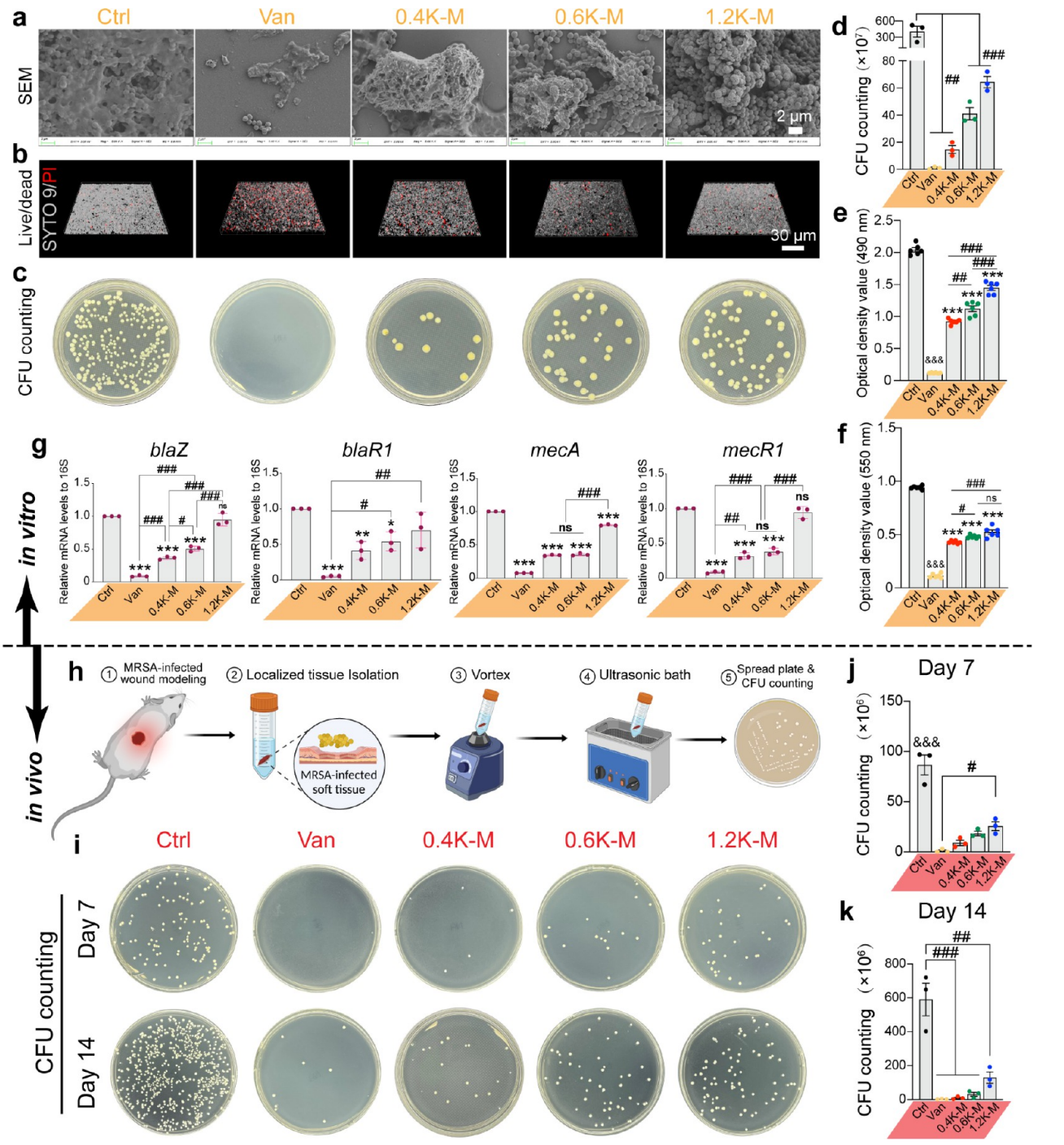

Figure 6. K-MnO_2 NPs effects on resisting MRSA *in vitro* and *in vivo*. a) K-MnO_2 NPs effects on the morphology of MRSA biofilms detected by SEM (scale bar: 2 μm). b) K-MnO_2 NPs effects on bacterial live/dead staining detected by CLSM (scale bar: 30 μm). c) K-MnO_2 NPs effects on the growth of MRSA colonies detected by spread plate assay and d) relevant analysis. e) MTT assay is measured at 490 nm wavelength. f) CV staining is measured at 550 nm wavelength. g) K-MnO_2 NPs effects on the expression of MRSA antibiotic-resistant genes. h) A flowchart outlines the detection of resisting MRSA *in vivo* by spread plate assay (created in BioRender. https://BioRender.com/k36m258). i) Images of the spread plate and j, k) statistical analyses of CFU counting on postoperative days 7 and 14 *in vivo*, respectively. The yellow-colored frames represent the diabetic culture setting. The red-colored frames represent the D/M culture setting. *$p < 0.05$; **$p < 0.01$; ***$p < 0.001$ as compared to Ctrl. $^{\#}p < 0.05$; $^{\#\#}p < 0.01$; $^{\#\#\#}p < 0.001$. $^{\&\&\&}p < 0.001$ as compared to the other groups.

neutrophils rapidly declined within 36 h and altogether ceased within 48 h (Figure 4f,g).

2.4. K-MnO_2 NPs Reprogram Neutrophil Sequential Behaviors Mediated by the Activation of Initial Ca^{2+} Influx in the D/M Setting. *2.4.1. K-MnO_2 NPs Trigger a Low-to-High Shift of Neutrophil Chemotaxis during 0–12 h.* Within 12 h, RT-qPCR was conducted to detect the expression of chemotactic signals (*Cxcl1* and *Cxcl5*) released by fibroblasts (Figure 5b,c), which was markedly reduced in the D/M setting ($p < 0.001$). Compared with 0.4K-M and Van, 1.2K-M and 0.6K-M significantly enhanced *Cxcl1* expression ($p < 0.01$), with 0.4K-M exhibiting higher expression compared to Van ($p <$

https://doi.org/10.1021/acsnano.4c14057
ACS Nano 2025, 19, 11807−11822

0.01). Additionally, 0.4K-M seemed particularly effective in increasing *Cxcl5* expression, especially compared to 1.2K-M ($p < 0.05$). Meanwhile, it was evident that neutrophil chemotaxis was significantly impeded in the Ctrl group within 12 h (Figure 5d). Conversely, 0.4K-M appeared to recruit the highest number of neutrophils in the D/M setting, with a statistically significant increase compared to Ctrl ($p < 0.01$) and 1.2K-M ($p < 0.05$; Figure 5e).

2.4.2. K-MnO_2 NPs Trigger a Low-to-High Shift of Intracellular ROS Generation during 0−12 h. Intracellular ROS levels generated in neutrophils during the initial 24 h are shown in Figure 5f. As expected, the Blk group greatly elevated intracellular ROS levels within 24 h, indicating a rapid response of neutrophil oxidative stress to MRSA infection. Conversely, the D/M setting (Ctrl) notably inhibited ROS generation within 24 h. Compared with Van and the other two NPs, 0.4K-M significantly enhanced ROS levels via a low-to-high shift within 12 h ($p < 0.001$).

2.4.3. K-MnO_2 NPs Trigger a Low-to-High Shift of NETosis during 0−12 h. NETosis is a major weapon for neutrophils to resist pathogens.[31] During 0−12 h intervals, the study systematically examined the *in vitro* and *in vivo* expression of PAD4 and H3-cit, two factors indispensable for NETosis. The combined results of WB, RT-qPCR, IF/ICC, and IHC revealed that PAD4 and H3-cit were substantially suppressed in the D/M setting (Figures 5g−l, 7a, S7c and S8c). Van significantly activated the expression of H3-cit (Figures 5h and S8c), but it was not synchronized with the expression of PAD4 (Figures 5i and S7c). In contrast, 0.4K-M was able to upregulate the expressions of H3-cit and PAD4 synchronously and thus activate PAD4-mediated NETosis. During the same period, 0.6K-M and 1.2K-M did not show an obvious effect on activating NETosis.

2.5. K-MnO_2 NPs Effects on Resisting MRSA *In Vitro* and *In Vivo*. In Figure S4a−f, the study found that *in vitro* and *in vivo*, a diabetic setting led to the rapid formation and maturation of MRSA biofilms. The morphologies of MRSA biofilms were observed by SEM (Figure 6a), revealing denser biofilms in the Ctrl group, while those in the Van group appeared severely damaged with fragmented morphologies. K-MnO_2 NPs were effective in disrupting the integrity of MRSA biofilms. Among all K-MnO_2 NPs, 0.4K-M exhibited optimal resistance against MRSA, with no significant difference between 0.4K-M and Van regarding bactericidal effect (Figure S6a). While 0.6K-M and 1.2K-M effectively inhibited MRSA biofilms compared to Ctrl, they were less effective than 0.4K-M and Van in this regard. Moreover, the live/dead staining results were consistent with these findings (Figure 6b). *In vitro* results of spread plate assay illustrated that both Van and 0.4K-M displayed optimal inhibitory effects on MRSA compared to the other groups ($p < 0.01$; Figure 6c,d), which was further supported by the MTT assay and CV staining (Figure 6e,f). Compared to the other groups, the Ctrl group particularly stimulated the growth of MRSA colonies *in vivo* ($p < 0.001$; Figure 6i). At each time point, among the K-MnO_2 NPs, 0.4K-M demonstrated the most pronounced efficacy in resisting MRSA. Upon considering the CFU counting analysis, no statistical difference was observed between 0.4K-M and the other NPs (Figure 6j,k). However, upon considering the result of the bactericidal coefficient, a significant statistical difference was observed between 0.4K-M and 1.2K-M ($p < 0.05$ on Day 7, $p < 0.01$ on Day 14; Figure S6b,c).

2.6. Antibiotic-Resistant Gene Expressions of MRSA in Response to K-MnO_2 NPs. Genes including *blaZ*, *blaR1*, *mecA*, and *mecR1* are critical for MRSA to resist antibiotics and maintain virulence. Expression of these genes was highest in Ctrl, particularly *mecA* ($p < 0.001$), suggesting that the diabetic setting favored MRSA survival (Figure 6g). Compared with Ctrl, most groups (except 1.2K-M) showed a significant reduction in the expression of *blaZ*, *blaR1*, and *mecR1*. Additionally, 1.2K-M also appeared to inhibit MRSA viability. Van dramatically inhibited the expression of all four genes, especially *blaZ* and *mecR1* ($p < 0.001$, $p < 0.01$). Compared with 0.6K-M, 0.4K-M significantly inhibited the expression of *blaZ* ($p < 0.05$). Also, the inhibitory effects of 0.4K-M and 0.6K-M on *blaZ*, *mecA*, and *mecR1* expression were superior to those of 1.2K-M ($p < 0.001$).

2.7. K-MnO_2 NPs Reprogram Neutrophil Sequential Behaviors Mediated by the Restored Calcium Homeostasis in the D/M Setting. *2.7.1. K-MnO_2 NPs Induce a High-to-Low Shift of Intracellular ROS Generation and NETosis during 12−24 h.* During the 0−12 h interval, the intracellular ROS significantly increased with a low-to-high shift in 0.4K-M. However, it decreased with a high-to-low shift during the 12−24 h interval. Van, 0.6K-M, and 1.2K-M continuously stimulated the generation of ROS within 24 h and exceeded 0.4K-M during the 12−24 h interval (Figure 5f). These two different patterns of changes were also observed in H3-cit and PAD4 (Figure 7a−f). Van still exhibited asynchronous expressions between H3-cit and PAD4 (Figures 7c, S7d and S8d).

2.7.2. K-MnO_2 NPs Induce a Low-to-High Shift of Neutrophil "Find-Me" Signals during 12−24 h. Within 24 h of infection, the D/M setting significantly reduced the expression of "find-me" signals, including *Cx3cl1* and *Icam3*, compared with the normal setting ($p < 0.01$; Figure 7g, h). During the 0−12 h interval, 0.4K-M was the most potent in suppressing all "find-me" signals compared with other groups, indicating that it could effectively block neutrophil apoptosis at the early stage, followed by the inhibitory effect of Van on *Cx3cl1* and *Icam3* expressions. Except for *Icam3*, there was no significant difference between 0.6K-M and 1.2K-M in the expression of *Cx3cl1* and ATP. However, during the 12−24 h interval, 0.4K-M upregulated the expression of "find-me" signals as a whole and was higher than that of all the other groups. Among them, the ATP level in the 0.4K-M group was significantly higher than that in Van group (Figure 7g−i). This low-to-high shift was conducive to the rapid clearance of apoptotic neutrophils, thereby promoting tissue repair.

2.7.3. Evaluation of Bactericidal Ability of Neutrophils Mediated by K-MnO_2 NPs in the D/M Setting during 12−24 h. The study further examined the *in vitro* inhibitory effect of neutrophils activated by K-MnO_2 NPs on MRSA after 24-h of coculturing in the D/M setting (Figure S5a). The *in vivo* and *in vitro* results indicated that the D/M setting significantly promoted the growth of MRSA colonies in the presence of neutrophils compared with Blk (Figure S5b). Both Van and 0.4K-M substantially inhibited the growth of MRSA colonies compared with the other groups (Figures S5c,d and S6d). Specifically, different K-MnO_2 NPs effectively killed MRSA within 24 h. 0.4K-M showed the highest inhibition of MRSA colonies among the K-MnO_2 NPs, thus demonstrating a reliable ability to resist MRSA within 24 h cocultured with neutrophils.

2.8. K-MnO_2 NPs Effects on Wound Healing *In Vitro* and *In Vivo*. The effects of K-MnO_2 NPs on wound healing were systematically evaluated both *in vitro* and *in vivo*. From an *in vitro* perspective, it was found that the D/M setting (Ctrl) substantially sabotaged the healing process compared to the other groups at 12 and 24 h. In contrast, both Van and 0.4K-M

https://doi.org/10.1021/acsnano.4c14057
ACS Nano 2025, 19, 11807−11822

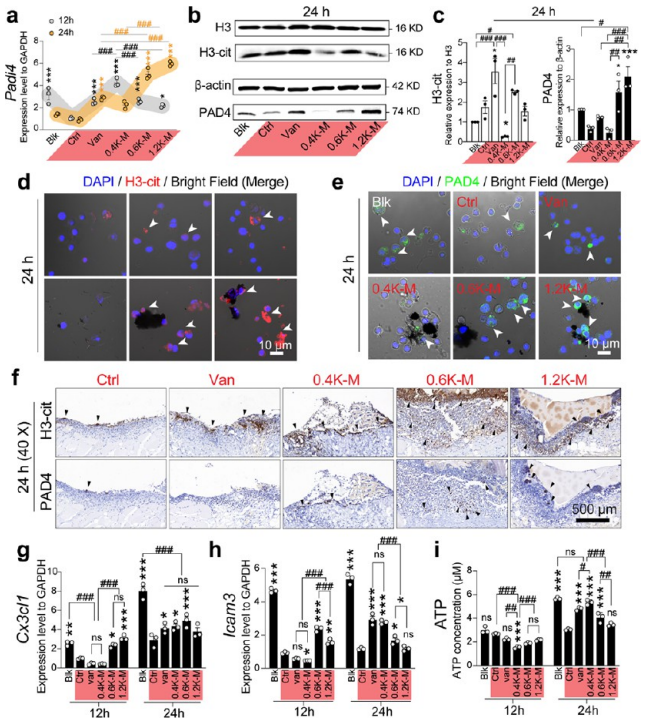

Figure 7. K-MnO_2 NPs reprogram neutrophil sequential behaviors mediated by the restored calcium homeostasis in the D/M setting. a) K-MnO_2 NPs effects on neutrophil *Padi4* expression in the D/M setting at 12, 24 h. b) WB images of H3-cit and PAD4 expressions at 24 h in the D/M setting, with c) relevant statistical analyses. d, e) IF/ICC images of H3-cit and PAD4 expressions in the D/M setting at 24 h *in vitro* (scale bar: 10 μm). f) IHC staining images of H3-cit and PAD4 expressions in the D/M setting at 24 h *in vivo* (scale bar: 500 μm). g-i) The expression of neutrophil "find-me" signals (*Cx3xl1*, *Icam3*, and ATP) at 12, 24 h in the D/M setting, respectively. The red-colored frames represent the D/M culture setting. $^{*}p < 0.05$; $^{**}p < 0.01$; $^{***}p < 0.001$ as compared to Ctrl. $^{\#}p < 0.05$; $^{\#\#}p < 0.01$; $^{\#\#\#}p < 0.001$.

promoted greater formation of healing areas after injury (Figures 8a and S9a,b), with 0.4K-M superior to 1.2K-M at 24 h ($p < 0.01$; Figure S9b). Herein, no significant difference was observed between 0.6K-M and 1.2K-M. As shown in Figure S9e–g, the D/M setting disrupted the expression of fibroblast repair genes including *Cxcl10*, *Cxcl11*, and *Cxcr3*. Compared with Ctrl, the protective effect of 0.4K-M was the most pronounced as it upregulated the expression of all repair-promoting genes in the presence of neutrophils ($p < 0.001$), especially in terms of *Cxcl11* and *Cxcr3* expressions compared with Van ($p < 0.001$). No statistical difference was observed between 0.6K-M and 1.2K-M.

As shown in Figure 8b, the D/M setting significantly increased the expression of all pro-inflammatory genes ($p < 0.01$) and suppressed the expression of the anti-inflammatory gene *Il-10* ($p < 0.001$) in fibroblasts over 24 h. There was no significant difference between the positive control and 0.4K-M in *Tnf-α*, *Mmp9*, and *Il-1β* expressions. Compared with Ctrl, 0.4K-M demonstrated favorable anti-inflammatory effects on the expression of *Tnf-α* ($p < 0.01$), *Mmp9* ($p < 0.05$), *Il-1β* ($p < 0.05$), *Il-6* ($p < 0.001$), and *Il-10* ($p < 0.01$). The 0.6K-M group exhibited some therapeutic effects by significantly inhibiting the expression of *Tnf-α*, *Il-1β*, and *Il-6*. The 1.2K-M group appeared to be effective in mitigating inflammation, whereas it significantly reduced the expression of *Il-10* compared with the 0.4K-M group ($p < 0.001$).

Next, considering the *in vivo* aspect, the diabetic rats were successfully modeled at first (Figure 8d,e). At baseline, there was no significant statistical difference in wounded area, perimeter, and Feret's diameter (Figure S9c). On days 7 and 14 postoperatively (Figure 8f–k; S9d), the process of skin healing was impeded in the Ctrl group. In contrast, by day 14, most of the injured skin had been replaced by fresh soft tissue in both the positive control (Van) and the 0.4K-M group ($p < 0.01$; Figure 8g,h), which was in accordance with the provided healing parameters (Figure 8i–k). In the 0.6K-M group, a thin layer of soft tissue covered the wounds, while some deeper tissue remained exposed in the 1.2K-M group. Furthermore, histological analysis through H&E staining and Masson staining showed that, in the Ctrl group, fibrous connective tissues predominated and covered the uppermost layer, accompanied by a heavy infiltration of numerous inflammatory cells (Figure 8l,m). Conversely, within the Van and 0.4K-M groups, a remarkable progression of wound healing was evident. The normal epithelial tissue was undergoing continuous repair, and a significant neovascularization stimulation was occurring. Notably, the expression of CD31, a key marker for newly formed blood vessels, was significantly enhanced in these two groups (Figure 8n,o). In the 0.6K-M and the 1.2K-M groups, some fibrous tissue was observed to proliferate and differentiate into epithelial tissue, but the connective tissue had fewer new vessels compared to the Van and the 0.4K-M groups.

3. DISCUSSION

Nanomaterials based on metal oxide semiconductors have emerged as a promising alternative approach in antimicrobial and tissue-repairing applications.[32−35] Suffering from poor electrical conductivity, the pro-healing performance of pristine MnO_2 no longer meets the rapidly evolving demands of clinical treatment.[36] Considering this, our study employed $KMnO_4$ as the precursor to synthesize semiconductive K-MnO_2 NPs via the hydrothermal method, known for its suitability for large-scale industrial production.[37] Based on the results of the materials' characteristics, they confirmed successful doping of the MnO_2 nanolayers with varying concentrations of K ions (Figure 2b,c), resulting in a distinct type of K-MnO_2 semiconductors (Figure 2f). Thus, the introduction of K ions improved the conductivity of MnO_2. More specifically, 0.4K-M and 0.6K-M (N-type) exhibited higher conductivity than 1.2K-M (P-type) due to their narrower bandgaps and lower binding energy (Figure S2a and Table 1).[38] Particularly, 0.4K-M appeared to fully activate its therapeutic potential. It was indicated that doping K ions at different ratios fundamentally altered the intrinsic conductivity of semiconductors. Among them, the doping ratio of 0.4K-M seemed optimal, as higher concentrations of oxygen vacancies were detected on its surface (Figure 2h), which facilitated the generation of ROS to eliminate pathogens,[39−41] Furthermore, 0.4K-M exhibited good biocompatibility both *in vitro* and *in vivo*, demonstrating broad application prospects for this nanoparticle (Figure S1).[42−45] However, when the amount of doped K ions exceeded a certain threshold, the therapeutic effects of K-MnO_2 seemed counterproductive. This requires further insights into the performance of different K-MnO_2 NPs at inflammatory wounds.

Within inflammatory wounds, neutrophils are the first-line innate immune cells that combat pathogens and initiate acute wound repair.[46,47] This complex process involves a variety of

https://doi.org/10.1021/acsnano.4c14057
ACS Nano 2025, 19, 11807−11822

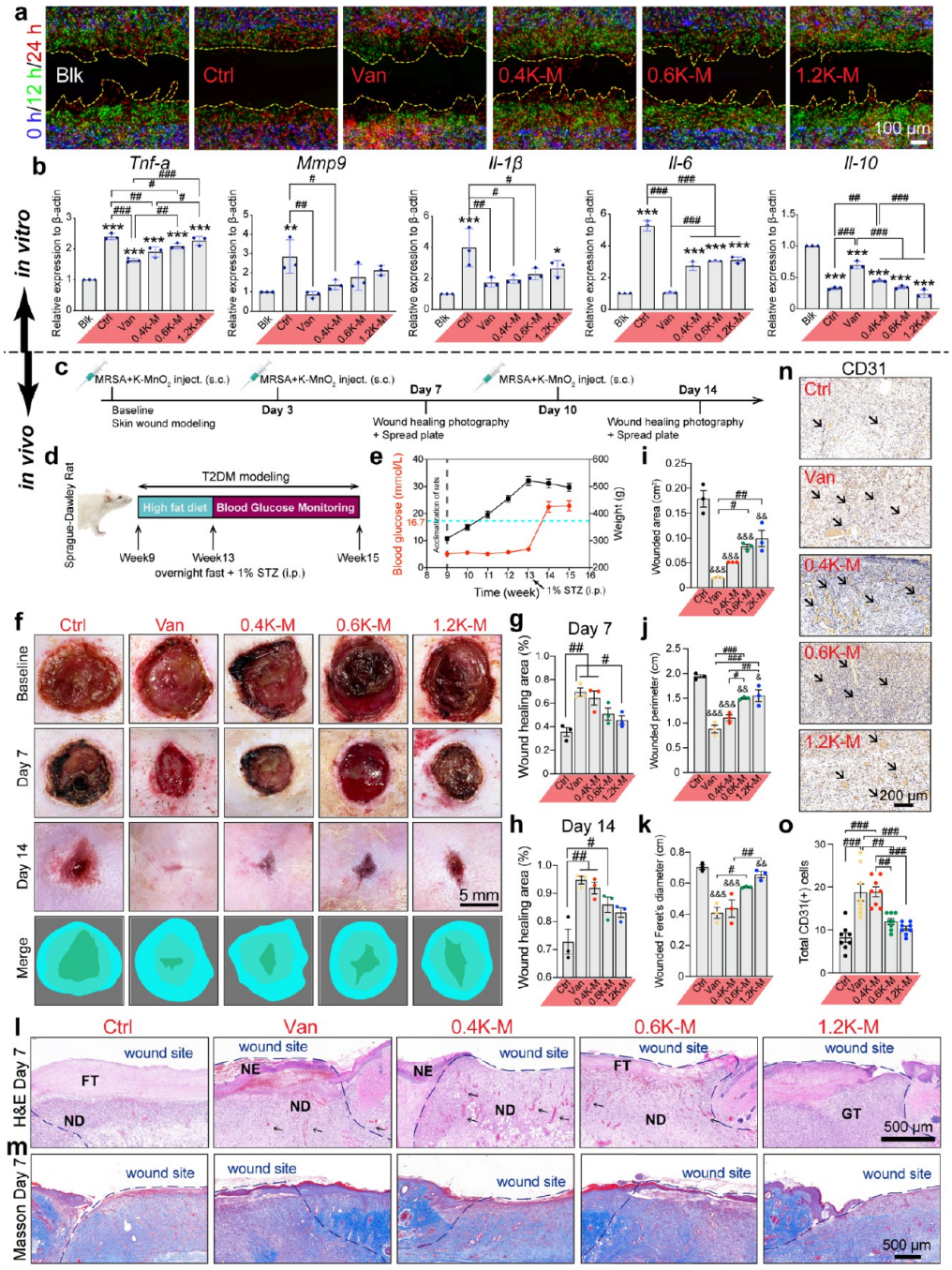

Figure 8. K-MnO_2 NPs effects on wound healing *in vitro* and *in vivo*. a) K-MnO_2 NPs effects on fibroblast migration at wounded sites in the D/M setting are depicted at 0, 12, and 24 h (scale bar: 100 μm). b) K-MnO_2 NPs effects on the expression of fibroblast inflammatory genes in the D/M setting. c) A flowchart outlines each surgical step from baseline to postoperative day 14 in diabetic rats. d) A schematic diagram illustrates the modeling of diabetic rats. e) Monitoring of blood glucose and body weight in diabetic rats. f) Images display the healing progress of MRSA-infected diabetic wounds on days 7 and 14, with g, h) relevant statistical analyses. i-k) The healing parameters of wound sites on Day 14. l) H&E staining and m) Masson trichrome staining images of infected skin from diabetic rats on day 7 (scale bar: 500 μm). n) IHC staining of CD31 of infected skin from diabetic rats on day 7 (scale bar: 200 μm), and o) relevant statistical analysis. The red-colored frames represent the D/M culture setting. Abbreviation: FT, fibrous tissue; ND, neodermis; NE, neoepidermis; GT, granulation tissue; Arrow, new vessels. $^{*}p < 0.05$; $^{**}p < 0.01$; $^{***}p < 0.001$ as compared to Blk. $^{\&}p < 0.05$; $^{\&\&}p < 0.01$; $^{\&\&\&}p < 0.001$ as compared to Ctrl. $^{\#}p < 0.05$; $^{\#\#}p < 0.01$; $^{\#\#\#}p < 0.001$.

neutrophil behaviors, including chemotaxis, intracellular ROS generation, phagocytosis, and NETosis (Figures 5 and 7).[28] When the damaged tissue is infected, local fibroblasts release recruitment signals, triggering the rapid recruitment of patrolling neutrophils as the initial step of their antibacterial response.[48] However, in the D/M setting, the signal pathway for chemotaxis is blocked, thus disrupting the interaction between fibroblasts and neutrophils.[49,50] Our study found that K-MnO_2 NPs significantly enhanced the recruitment signals by increasing *Cxcl1* and *Cxcl5* expressions in fibroblasts (Figure 5b,c). Interestingly, the expression level of *Cxcl1* was higher at 0.6K-M and 1.2K-M compared to 0.4K-M, whereas *Cxcl5* exhibited an opposite expression pattern. This might be attributed to the distinct functions of CXC chemokines. *Cxcl1* acts as a potent

https://doi.org/10.1021/acsnano.4c14057
ACS Nano 2025, 19, 11807−11822

activator for neutrophil recruitment,[51] assisting damaged fibroblasts to manage localized inflammation. In contrast, *Cxcl5* shows greater potential in promoting angiogenesis and facilitating soft tissue repair.[52,53] Given the potent tissue-repairing and anti-inflammatory capabilities of 0.4K-M (Figures 8a,b and S9e−g), the upregulated expression of *Cxcl5* might imply that the diabetic wound is gradually transitioning from the inflammatory response phase to the repair phase. At this stage, K-MnO_2 of nanoscale could fully contact with the recruited neutrophils and activate them to participate in antibacterial activities through electron transfer.

However, the D/M setting can significantly suppress the membrane potential of neutrophils, leading to the recruited neutrophils entering a hibernation-like state.[48] Pathogens then utilize them as a "Trojan horse" to protect themselves, thus preventing neutrophils from further attacks and rendering the immune defense dysfunctional.[54] Our study found that MnO_2 with very limited electrical conductivity could not awaken neutrophils, while K-MnO_2 NPs were, on the contrary, able to wake up the hibernating neutrophils through electron transfer. Notably, within the first 12 h of the inflammatory phase, 0.4K-M NPs could transfer more electrons to neutrophils, allowing them to be more easily activated (Figure 4f,h,i). This would rapidly promote the activation of voltage-gated ion channels on the cell membrane,[55] which is vital for triggering the subsequent antibacterial responses. However, the exact types of ion channels activated on the cell membrane remain unknown. Elucidating this issue will reveal the immunomodulatory pattern of K-MnO_2 on neutrophils.

Herein, RNA sequencing was applied to identify the differentially expressed membrane proteins in neutrophils, providing valuable insights into the activated state of these cells. The results revealed significant alterations in various types of Ca^{2+} channels, namely T-type, L-type, N-type VGCC, and SOCs (Figure 3b). This led to a particular focus on Ca^{2+} signaling. In the D/M setting, the Ca^{2+} signaling pathway was notably suppressed within 12 h, severely disrupting the bactericidal functions of neutrophils.[56] Conversely, 0.4K-M with optimal conductivity was capable of activating a variety of key transmembrane Ca^{2+} channels from the start, which facilitated a rapid influx of Ca^{2+}. Notably, the activation of N-type channels, which are highly voltage-dependent VGCCs,[19] appeared to play a pivotal role in this process (Figure 4c,d). The latest research has pointed out that ORAI1 and ORAI2 in SOCE are dominant in activating calcium signaling in murine neutrophils.[57] Subsequently, the inflow of Ca^{2+} acted as a second messenger. It reprogrammed sequential Ca^{2+}-mediated behaviors via a low-to-high shift, such as intracellular ROS generation (Figure 5f) and PAD4-mediated NETosis (Figure 5g−l). These behaviors provided reliable defenses against both intracellular and extracellular MRSA at wound sites (Figure S6d),[16,58] suggesting that K-MnO_2 NPs leveraged hibernating neutrophils to underlie a robust defense against invading MRSA.

Furthermore, sustained Ca^{2+} influx led to calcium overload, resulting in prolonged neutrophil retention and NETs impeding tissue repair. Calcium homeostasis serves as an effective feedback system in neutrophils to mitigate calcium overload and dampen aggressive responses of apoptotic neutrophils.[59] Nevertheless, calcium homeostasis appeared dysfunctional due to MRSA infection.[60] Our study demonstrated that 0.4K-M was optimal for combating MRSA (Figure 6a−f), which was essential for eliminating infection to restore functional calcium homeostasis. This functional calcium homeostasis effectively curtailed Ca^{2+}-mediated ROS generation and NETosis during the wound healing period (Figures 5f and 7a−f). Meanwhile, 0.4K-M was observed to induce a low-to-high shift of "find-me" signals (*Cx3cl1*, *Icam3*, ATP) in apoptotic neutrophils at 24 h (Figure 7g−i),[61−63] This might be attributed to its ability to enable the rapid intracellular accumulation of ROS and subsequently activate apoptotic signals,[64−66] Owing to the coordination of these signals, apoptotic neutrophils and NETs could be efficiently expelled from the injury sites, which plays a crucial role in alleviating inflammation and promoting wound healing (Figure 8).

This study further investigated the interaction between Van, a first-line drug for MRSA infections, and innate immune defense. Our results highlighted significant differences between 0.4K-M and Van regarding the mechanism of NETosis. Van was not found to mediate PAD4-induced NETosis, while the high expression of extracellular histone, a key component of NETs, appeared to result from cellular component efflux postneutrophil death (Figures 5h, 7c and S8).[67] Consequently, Van seemed to rely solely on its bactericidal properties without harnessing the potent weapon of neutrophils (NETs), potentially exacerbating the reliance on antibiotics for infected wounds. In contrast, 0.4K-M fully exploited PAD4 for NET-mediated antimicrobial effects, termed functional NETosis.[68] Moreover, due to the prompt response of "find-me" signals, 0.4K-M was less susceptible to the adverse effects of NET retention. Compared to first-line antibiotics, these findings suggested that our advanced nanomaterials could enhance the reparative potential of impaired neutrophils in the D/M setting. Regarding MRSA resistance, the Van group exhibited superior suppression of key antibiotic-resistance genes compared to the 0.4K-M group (Figure 6g). This difference could be attributed to the fact that MRSA was exposed to Van only once in our study, at which time the resistance barrier had not yet been established.[69] However, repeated exposure to Van was expected to increase MRSA resistance,[70] which was not a concern with applying K-MnO_2 NPs.

A major objective of this study was to offer a nonantibiotic strategy for wound healing in the D/M setting. As a potential alternative to antibiotics, 0.4K-M NPs circumvent the issue of drug resistance development. Moreover, they can play a more constructive role by reprogramming calcium signaling to enhance neutrophil functions the pro-healing effect and antibacterial efficacy of neutrophils (Figure 1). Given these advantages, 0.4K-M NPs can be considered a "smart" strategy that transforms damaged neutrophils from "foes" to "friends", thereby promoting the healing of infected diabetic wounds.

4. STUDY LIMITATIONS

This study has several limitations and deficiencies that need to be pointed out. First, in the skin defect model of rats, the wound shape was not sufficiently consistent at baseline, which might raise concerns about its potential impact on the final healing results. In response to this, we have already demonstrated through analysis that there was no statistical difference among groups regarding the wound area, perimeter, and Feret's diameter. Second, it will be necessary to conduct further experiments to precisely quantify the electron loss of 0.4K-M NPs and determine the optimal number of electrons required to modulate the functional behaviors of neutrophils. Additionally, after neutrophils express the "find-me" signal, detecting the "eat-me" signal of neutrophils and observing the recruited macrophages by transmission electron microscope (TEM) can provide

https://doi.org/10.1021/acsnano.4c14057
ACS Nano 2025, 19, 11807−11822

insights into the clearance outcomes of neutrophils. These assessments will be refined in future research endeavors.

5. CONCLUSIONS

In conclusion, the study presented comprehensive evidence supporting the fabrication and application of novel semiconductive NPs, specifically K-MnO_2 NPs, as a therapeutic approach for wound healing in the D/M setting. By harnessing Ca^{2+} signaling via electron transfer, the representative semiconductor 0.4K-M NPs demonstrated the ability to modify various neutrophil behaviors, such as awakening hibernating neutrophils and establishing a robust barrier against MRSA invasion in diabetic wounds. Both *in vitro* and *in vivo* findings underscored the capacity of 0.4K-M NPs to rectify dysfunctional neutrophil chemotaxis, intracellular ROS generation, NETosis, and "find-me" signals promptly, facilitating bacterial elimination and expediting wound healing. A notable finding of this study is the ability of 0.4K-M NPs to activate initial Ca^{2+} influx and restore calcium homeostasis in damaged neutrophils. Overall, this study marks the first endeavor to highlight the reparative potential of impaired neutrophils in the D/M setting through advanced NP technology. The proposed strategy holds promise for reshaping the perception of neutrophils as "more friend than foe" in complex wound healing scenarios beyond diabetic wounds.

6. METHODS

6.1. Synthesis of K-MnO_2 NPs. K-MnO_2 NPs were prepared using the hydrothermal method. Specifically, 0.4, 0.6, and 1.2 g of the precursors $KMnO_4$ (>99.5%, Sinopharm, Shanghai, China), 0.4 g of $MnSO_4$ (Sigma-Aldrich) were mixed with 30 mL of double-distilled water (ddH_2O). The mixture was then stirred in a stainless-steel autoclave at 140 °C for 1 h. Afterward, each type of K-MnO_2 NPs (0.4K-M, 0.6K-M, 1.2K-M_2) was washed with ethanol and ddH_2O, then dried at 60 °C for 12 h.

6.2. Applied Concentration Screening of K-MnO_2 NPs. K-MnO_2 has been reported to be biocompatible at concentrations ≤ 800 μg mL^{-1} (ISO 10993−5:2009). Based on that, a pilot cytotoxicity screening was conducted using concentration gradients (100, 200, 400, and 800 μg mL^{-1}) through CCK-8 assay (C0038, Beyotime, China). The optimal NP concentration was determined by coculture experiments with L929 fibroblasts (CCL-1, ATCC, USA), which were maintained under standard culture conditions as previously described.[71]

ASSOCIATED CONTENT

Data Availability Statement

The data that support the findings of this study are available from the corresponding author upon reasonable request.

Supporting Information

The Supporting Information is available free of charge at https://pubs.acs.org/doi/10.1021/acsnano.4c14057.

Additional experimental details, methods, *in vitro*/*in vivo* data, and statistical analysis (PDF)

AUTHOR INFORMATION

Corresponding Authors

Hongchang Lai − *Department of Oral and Maxillofacial Implantology, Shanghai Ninth People's Hospital, Shanghai Jiao Tong University School of Medicine; College of Stomatology, Shanghai Jiao Tong University; National Center for Stomatology; National Clinical Research Center for Oral Diseases; Shanghai Key Laboratory of Stomatology; Shanghai Research Institute of Stomatology, Shanghai 200011, China;* orcid.org/0000-0002-6922-2918; Phone: 86-021-23271073; Email: lhc9@hotmail.com

Xin Liu − *Department of Dental Materials, Shanghai Biomaterials Research & Testing Center, Shanghai Ninth People's Hospital, Shanghai Jiao Tong University School of Medicine; College of Stomatology, Shanghai Jiao Tong University; National Center for Stomatology; National Clinical Research Center for Oral Diseases; Shanghai Key Laboratory of Stomatology, Shanghai 200011, China;* Email: liuxin8253@sjtu.edu.cn

Junyu Shi − *Department of Oral and Maxillofacial Implantology, Shanghai Ninth People's Hospital, Shanghai Jiao Tong University School of Medicine; College of Stomatology, Shanghai Jiao Tong University; National Center for Stomatology; National Clinical Research Center for Oral Diseases; Shanghai Key Laboratory of Stomatology; Shanghai Research Institute of Stomatology, Shanghai 200011, China;* orcid.org/0000-0002-8241-2572; Email: sjy0511@hotmail.com

Authors

Jianxu Wei − *Department of Oral and Maxillofacial Implantology, Shanghai Ninth People's Hospital, Shanghai Jiao Tong University School of Medicine; College of Stomatology, Shanghai Jiao Tong University; National Center for Stomatology; National Clinical Research Center for Oral Diseases; Shanghai Key Laboratory of Stomatology; Shanghai Research Institute of Stomatology, Shanghai 200011, China;* orcid.org/0000-0002-6384-0512

Xiaomeng Zhang − *Department of Oral and Maxillofacial Implantology, Shanghai Ninth People's Hospital, Shanghai Jiao Tong University School of Medicine; College of Stomatology, Shanghai Jiao Tong University; National Center for Stomatology; National Clinical Research Center for Oral Diseases; Shanghai Key Laboratory of Stomatology; Shanghai Research Institute of Stomatology, Shanghai 200011, China;* orcid.org/0000-0003-2504-8599

Baiyan Sui − *Department of Dental Materials, Shanghai Biomaterials Research & Testing Center, Shanghai Ninth People's Hospital, Shanghai Jiao Tong University School of Medicine; College of Stomatology, Shanghai Jiao Tong University; National Center for Stomatology; National Clinical Research Center for Oral Diseases; Shanghai Key Laboratory of Stomatology, Shanghai 200011, China;* orcid.org/0009-0009-7965-0746

Xinxin Ding − *Department of Oral and Maxillofacial Implantology, Shanghai Ninth People's Hospital, Shanghai Jiao Tong University School of Medicine; College of Stomatology, Shanghai Jiao Tong University; National Center for Stomatology; National Clinical Research Center for Oral Diseases; Shanghai Key Laboratory of Stomatology; Shanghai Research Institute of Stomatology, Shanghai 200011, China*

Yuan Li − *Department of Oral and Maxillofacial Implantology, Shanghai Ninth People's Hospital, Shanghai Jiao Tong University School of Medicine; College of Stomatology, Shanghai Jiao Tong University; National Center for Stomatology; National Clinical Research Center for Oral Diseases; Shanghai Key Laboratory of Stomatology; Shanghai Research Institute of Stomatology, Shanghai 200011, China;* orcid.org/0000-0002-0133-7516

https://doi.org/10.1021/acsnano.4c14057
ACS Nano 2025, 19, 11807−11822

Beilei Liu − *Department of Oral and Maxillofacial Implantology, Shanghai Ninth People's Hospital, Shanghai Jiao Tong University School of Medicine; College of Stomatology, Shanghai Jiao Tong University; National Center for Stomatology; National Clinical Research Center for Oral Diseases; Shanghai Key Laboratory of Stomatology; Shanghai Research Institute of Stomatology, Shanghai 200011, China;* orcid.org/0000-0002-6675-4054

Jiale Wang − *College of Physics and Shanghai Institute of Intelligent Electronics and Systems, Donghua University, Shanghai 201620, China*

Xiaolei Lv − *Department of Oral and Maxillofacial Implantology, Shanghai Ninth People's Hospital, Shanghai Jiao Tong University School of Medicine; College of Stomatology, Shanghai Jiao Tong University; National Center for Stomatology; National Clinical Research Center for Oral Diseases; Shanghai Key Laboratory of Stomatology; Shanghai Research Institute of Stomatology, Shanghai 200011, China;* orcid.org/0009-0002-7067-7044

Yi Zhang − *Department of Oral and Maxillofacial Implantology, Shanghai Ninth People's Hospital, Shanghai Jiao Tong University School of Medicine; College of Stomatology, Shanghai Jiao Tong University; National Center for Stomatology; National Clinical Research Center for Oral Diseases; Shanghai Key Laboratory of Stomatology; Shanghai Research Institute of Stomatology, Shanghai 200011, China;* orcid.org/0000-0002-6891-9262

Xue Jiang − *Department of Oral and Maxillofacial Implantology, Shanghai Ninth People's Hospital, Shanghai Jiao Tong University School of Medicine; College of Stomatology, Shanghai Jiao Tong University; National Center for Stomatology; National Clinical Research Center for Oral Diseases; Shanghai Key Laboratory of Stomatology; Shanghai Research Institute of Stomatology, Shanghai 200011, China;* orcid.org/0000-0003-1523-104X

Yijie Yang − *Department of Oral and Maxillofacial Implantology, Shanghai Ninth People's Hospital, Shanghai Jiao Tong University School of Medicine; College of Stomatology, Shanghai Jiao Tong University; National Center for Stomatology; National Clinical Research Center for Oral Diseases; Shanghai Key Laboratory of Stomatology; Shanghai Research Institute of Stomatology, Shanghai 200011, China;* orcid.org/0000-0003-0245-2433

Complete contact information is available at: https://pubs.acs.org/10.1021/acsnano.4c14057

Author Contributions

#J.W., X.Z., and B.S. contributed equally to this work. J.W. designed and performed experiments, analyzed data, wrote the manuscript, and had unrestricted access to all data. X.Z. analyzed data, critically reviewed the manuscript, and supported the funding. B.S. performed experiments and provided methodology. X.D., Y.L., and B.L. performed statistical analyses and supported the funding. J.W. designed the study and provided the biomaterials. X.L., Y.Z., X.J., and Y.Y. performed statistical analyses. X.L.* provided methodology and reviewed the manuscript. H.L.* and J.S.* designed the study and experiments, supported the funding, and had unrestricted access to all data. All authors read and approved the final article and take responsibility for its content.

Notes

The authors declare no competing financial interest.

ACKNOWLEDGMENTS

This work was supported by the National Natural Science Foundation of China (Grant numbers: 82271028, 82171005, 82201094, 82100964), Shanghai Rising-Star Program (Grant number: 22QA1405200), Shanghai Pujiang Program (Grant number: 22PJD038), Shanghai Young Talents in Healthcare (Grant number: 2022YQ041), Cross-disciplinary Research Fund of Shanghai Ninth People's Hospital, Shanghai Jiao Tong University School of Medicine (Grant number: JYJC202205), Biomaterials and Regenerative Medicine Institute Cooperative Research Project by Shanghai Jiao Tong University School of Medicine (Grant number: 2022LHB03), and Biobank Project of Ninth People's Hospital Affiliated Shanghai Jiao Tong University School of Medicine (Grant number: YBKA202207). We acknowledge BioRender.com for providing selected icons used in this study.

REFERENCES

(1) Chen, Z.; Song, S.; Zeng, H.; Ge, Z.; Liu, B.; Fan, Z. 3d Printing Mof Nanozyme Hydrogel with Dual Enzymatic Activities and Visualized Glucose Monitoring for Diabetic Wound Healing. *Chem. Eng. J.* **2023**, *471*, 144649.

(2) Zhang, X.; Wang, Z.; Jiang, H.; Zeng, H.; An, N.; Liu, B.; Sun, L.; Fan, Z. Self-Powered Enzyme-Linked Microneedle Patch for Scar-Prevention Healing of Diabetic Wounds. *Sci. Adv.* **2023**, *9*, No. eadh1415.

(3) Tan, W.; Long, T.; Wan, Y.; Li, B.; Xu, Z.; Zhao, L.; Mu, C.; Ge, L.; Li, D. Dual-Drug Loaded Polysaccharide-Based Self-Healing Hydrogels with Multifunctionality for Promoting Diabetic Wound Healing. *Carbohydr. Polym.* **2023**, *312*, 120824.

(4) Tu, Z.; Zhong, Y.; Hu, H.; Shao, D.; Haag, R.; Schirner, M.; Lee, J.; Sullenger, B.; Leong, K. W. Design of Therapeutic Biomaterials to Control Inflammation. *Nat. Rev. Mater.* **2022**, *7*, 557−574.

(5) Selders, G. S.; Fetz, A. E.; Radic, M. Z.; Bowlin, G. L. An Overview of the Role of Neutrophils in Innate Immunity, Inflammation and Host-Biomaterial Integration. *Regener. Biomater.* **2017**, *4*, 55−68.

(6) Peiseler, M.; Kubes, P. More Friend Than Foe: The Emerging Role of Neutrophils in Tissue Repair. *J. Clin. Invest.* **2019**, *129*, 2629−2639.

(7) Filep, J. G. Targeting Neutrophils for Promoting the Resolution of Inflammation. *Front. Immunol.* **2022**, *13*, 866747.

(8) Frenkel, J. S. The Role of Hyaluronan in Wound Healing. *Int. Wound J.* **2014**, *11*, 159−163.

(9) Jiang, D.; Liang, J.; Noble, P. W. Hyaluronan as an Immune Regulator in Human Diseases. *Physiol. Rev.* **2011**, *91*, 221−264.

(10) Patil, S. D.; Papadimitrakopoulos, F.; Burgess, D. J. Dexamethasone-Loaded Poly(Lactic-Co-Glycolic) Acid Microspheres/Poly(Vinyl Alcohol) Hydrogel Composite Coatings for Inflammation Control. *Diabetes Technol. Ther.* **2004**, *6*, 887−897.

(11) Morais, J. M.; Papadimitrakopoulos, F.; Burgess, D. J. Biomaterials/Tissue Interactions: Possible Solutions to Overcome Foreign Body Response. *AAPS J.* **2010**, *12*, 188−196.

(12) Singer, M. The Role of Mitochondrial Dysfunction in Sepsis-Induced Multi-Organ Failure. *Virulence* **2014**, *5*, 66−72.

(13) Rocha, J. L. L.; Kondo, W.; Baptista, M. I. D. K.; Da Cunha, C. A.; Martins, L. T. F. Uncommon vancomycin: Induced side effects. *Braz. J. Infect. Dis.* **2002**, *6*, 196−200.

(14) Parker, H.; Dragunow, M.; Hampton, M. B.; Kettle, A. J.; Winterbourn, C. C. Requirements for Nadph Oxidase and Myeloperoxidase in Neutrophil Extracellular Trap Formation Differ Depending on the Stimulus. *J. Leukoc. Biol.* **2012**, *92*, 841−849.

(15) Douda, D. N.; Khan, M. A.; Grasemann, H.; Palaniyar, N. Sk3 Channel and Mitochondrial Ros Mediate Nadph Oxidase-Independent Netosis Induced by Calcium Influx. *Proc. Natl. Acad. Sci. U. S. A.* **2015**, *112*, 2817−2822.

(16) Hann, J.; Bueb, J. L.; Tolle, F.; Brechard, S. Calcium Signaling and Regulation of Neutrophil Functions: Still a Long Way to Go. *J. Leukoc. Biol.* **2020**, *107*, 285−297.
(17) Dunyach-Remy, C.; Ngba Essebe, C.; Sotto, A.; Lavigne, J. P. Staphylococcus aureus Toxins and Diabetic Foot Ulcers: Role in Pathogenesis and Interest in Diagnosis. *Toxins* **2016**, *8*, 209.
(18) Yano, H.; Kinoshita, M.; Fujino, K.; Nakashima, M.; Yamamoto, Y.; Miyazaki, H.; Hamada, K.; Ono, S.; Iwaya, K.; Saitoh, D.; Seki, S.; Tanaka, Y. Insulin Treatment Directly Restores Neutrophil Phagocytosis and Bactericidal Activity in Diabetic Mice and Thereby Improves Surgical Site Staphylococcus aureus Infection. *Infect. Immun.* **2012**, *80*, 4409−4416.
(19) Catterall, W. A. Voltage-Gated Calcium Channels. *Cold Spring Harbor Perspect. Biol.* **2011**, *3*, a003947.
(20) Wang, D.; Tan, J.; Zhu, H.; Mei, Y.; Liu, X. Biomedical Implants with Charge-Transfer Monitoring and Regulating Abilities. *Adv. Sci.* **2021**, *8*, No. e2004393.
(21) Sikora, P.; Augustyniak, A.; Cendrowski, K.; Nawrotek, P.; Mijowska, E. Antimicrobial Activity of Al2O3, CuO, Fe3O4, and ZnO Nanoparticles in Scope of Their Further Application in Cement-Based Building Materials. *Nanomaterials* **2018**, *8*, 212.
(22) Hu, S.; Liu, X.; Wang, C.; Camargo, P. H. C.; Wang, J. Tuning Thermal Catalytic Enhancement in Doped Mno(2)-Au Nano-Heterojunctions. *ACS Appl. Mater. Interfaces* **2019**, *11*, 17444−17451.
(23) Yan, Y.; Jiang, N.; Liu, X.; Pan, J.; Li, M.; Wang, C.; Camargo, P. H. C.; Wang, J. Enhanced Spontaneous Antibacterial Activity of δ-MnO2 by Alkali Metals Doping. *Front. Bioeng. Biotechnol.* **2022**, *9*, 788574.
(24) Saeed, M.; Ilyas, M.; Siddique, M.; Ahmad, A. Oxidative Degradation of Oxalic Acid in Aqueous Medium Using Manganese Oxide as Catalyst at Ambient Temperature and Pressure. *Arabian J. Sci. Eng.* **2013**, *38*, 1739−1748.
(25) Luo, J.; Zhang, Q.; Suib, S. L. Mechanistic and Kinetic Studies of Crystallization of Birnessite. *Inorg. Chem.* **2000**, *39*, 741−747.
(26) Gupta, V. K.; Fakhri, A.; Azad, M.; Agarwal, S. Synthesis and Characterization of Ag Doped Zns Quantum Dots for Enhanced Photocatalysis of Strychnine Asa Poison: Charge Transfer Behavior Study by Electrochemical Impedance and Time-Resolved Photoluminescence Spectroscopy. *J. Colloid Interface Sci.* **2018**, *510*, 95−102.
(27) Zhang, Z.; Feng, C.; Wang, D.; Zhou, S.; Wang, R.; Hu, S.; Li, H.; Zuo, M.; Kong, Y.; Bao, J.; et al. Selectively Anchoring Single Atoms on Specific Sites of Supports for Improved Oxygen Evolution. *Nat. Commun.* **2022**, *13*, 2473.
(28) Pillay, J.; den Braber, I.; Vrisekoop, N.; Kwast, L. M.; de Boer, R. J.; Borghans, J. A.; Tesselaar, K.; Koenderman, L. In Vivo Labeling with 2h2o Reveals a Human Neutrophil Lifespan of 5.4 Days. *Blood* **2010**, *116*, 625−627.
(29) Khoyratty, T. E.; Ai, Z.; Ballesteros, I.; Eames, H. L.; Mathie, S.; Martin-Salamanca, S.; Wang, L.; Hemmings, A.; Willemsen, N.; von Werz, V.; Zehrer, A.; Walzog, B.; van Grinsven, E.; Hidalgo, A.; Udalova, I. A. Distinct Transcription Factor Networks Control Neutrophil-Driven Inflammation. *Nat. Immunol.* **2021**, *22*, 1093−1106.
(30) Xiao, X.; Zhang, Z.; Wu, Y.; Xu, J.; Gao, X.; Xu, R.; Huang, W.; Ye, Y.; Oyakhire, S. T.; Zhang, P.; et al. Ultrahigh-Loading Manganese-Based Electrodes for Aqueous Batteries Via Polymorph Tuning. *Adv. Mater.* **2023**, *35*, No. e2211555.
(31) Ríos-López, A. L.; González, G. M.; Hernández-Bello, R.; Sánchez-González, A. Avoiding the Trap: Mechanisms Developed by Pathogens to Escape Neutrophil Extracellular Traps. *Microbiol. Res.* **2021**, *243*, 126644.
(32) Fan, Y.; Wang, Z.; Ren, W.; Liu, G.; Xing, J.; Xiao, T.; Li, W.; Li, Y.; Yu, P.; Ning, C.; Song, Z. Space-Confined Synthesis of Thin Polypyrrole Nanosheets in Layered Bismuth Oxychloride for a Photoresponse Antibacterial within the Near-Infrared Window and Accelerated Wound Healing. *ACS Appl. Mater. Interfaces* **2022**, *14*, 36966−36979.
(33) Weng, Z.; Xu, Y.; Gao, J.; Wang, X. Research Progress of Stimuli-Responsive Zno-Based Nanomaterials in Biomedical Applications. *Biomater. Sci.* **2022**, *11*, 76−95.
(34) Moccia, F.; Negri, S.; Faris, P.; Ronchi, C.; Lodola, F. Optical Excitation of Organic Semiconductors as a Highly Selective Strategy to Induce Vascular Regeneration and Tissue Repair. *Vasc. Pharmacol.* **2022**, *144*, 106998.
(35) Zhang, L.; Pornpattananangku, D.; Hu, C. M.; Huang, C. M. Development of Nanoparticles for Antimicrobial Drug Delivery. *Curr. Med. Chem.* **2010**, *17*, 585−594.
(36) Song, X.; Wang, H.; Li, Z.; Du, C. F.; Guo, R. A Review of MnO 2 Composites Incorporated with Conductive Materials for Energy Storage. *Chem. Rec.* **2022**, *22*, No. e202200118.
(37) Liu, W.; Wang, S.; Wang, J.; Zhang, B.; Liu, L.; Liu, H.; Yang, J. Supercritical Hydrothermal Synthesis of Nano-Zinc Oxide: Process and Mechanism. *Ceram. Int.* **2022**, *48*, 22629−22646.
(38) Nagarajan, K.; George, J.; Thomas, A.; Devaux, E.; Chervy, T.; Azzini, S.; Joseph, K.; Jouaiti, A.; Hosseini, M. W.; Kumar, A.; Genet, C.; Bartolo, N.; Ciuti, C.; Ebbesen, T. W. Conductivity and Photoconductivity of a P-Type Organic Semiconductor under Ultrastrong Coupling. *ACS Nano* **2020**, *14*, 10219−10225.
(39) Hao, Y. J.; Liu, B.; Tian, L. G.; Li, F. T.; Ren, J.; Liu, S. J.; Liu, Y.; Zhao, J.; Wang, X. J. Synthesis of 111 Facet-Exposed Mgo with Surface Oxygen Vacancies for Reactive Oxygen Species Generation in the Dark. *ACS Appl. Mater. Interfaces* **2017**, *9*, 12687−12693.
(40) Lakshmi Prasanna, V.; Vijayaraghavan, R. Insight into the Mechanism of Antibacterial Activity of Zno: Surface Defects Mediated Reactive Oxygen Species Even in the Dark. *Langmuir* **2015**, *31*, 9155−9162.
(41) An, G.; Zhu, J.; Huang, Q.; Gu, M.; Sun, Y.; Xu, L.; Tao, T.; Yang, B.; Chen, M.; Yang, H. Synergistic Effect of Photo-Thermal Oxidation for a Low Concentration of Hcho over Bi(3+)-Tio(2)/Mnfeo(X) Catalysts at Ambient Temperature. *Environ. Sci. Pollut. Res. Int.* **2023**, *30*, 10191−10201.
(42) Taranu, B.-O.; Novaconi, S. D.; Ivanovici, M.; Gonçalves, J. N.; Rus, F. S. A-Mno2 Nanowire Structure Obtained at Low Temperature with Aspects in Environmental Remediation and Sustainable Energy Applications. *Appl. Sci.* **2022**, *12*, 6821.
(43) Zhao, X.; Guo, B.; Wu, H.; Liang, Y.; Ma, P. X. Injectable Antibacterial Conductive Nanocomposite Cryogels with Rapid Shape Recovery for Noncompressible Hemorrhage and Wound Healing. *Nat. Commun.* **2018**, *9*, 2784.
(44) Poyraz, S.; Cerkez, I.; Huang, T. S.; Liu, Z.; Kang, L.; Luo, J.; Zhang, X. One-Step Synthesis and Characterization of Polyaniline Nanofiber/Silver Nanoparticle Composite Networks as Antibacterial Agents. *ACS Appl. Mater. Interfaces* **2014**, *6*, 20025−20034.
(45) Liang, T.; Zeng, L.; Shi, Y.; Pan, H.; Chu, P. K.; Yeung, K. W. K.; Zhao, Y. In Vitro and in Vivo Antibacterial Performance of Zr & O Piii Magnesium Alloys with High Concentration of Oxygen Vacancies. *Bioact. Mater.* **2021**, *6*, 3049−3061.
(46) Wilgus, T. A.; Roy, S.; McDaniel, J. C. Neutrophils and Wound Repair: Positive Actions and Negative Reactions. *Adv. Wound Care* **2013**, *2*, 379−388.
(47) Patangia, D. V.; Anthony Ryan, C.; Dempsey, E.; Paul Ross, R.; Stanton, C. Impact of Antibiotics on the Human Microbiome and Consequences for Host Health. *MicrobiologyOpen* **2022**, *11*, No. e1260.
(48) Wang, J. Neutrophils in Tissue Injury and Repair. *Cell Tissue Res.* **2018**, *371*, 531−539.
(49) Campbell, A. E.; McCready-Vangi, A. R.; Uberoi, A.; Murga-Garrido, S. M.; Lovins, V. M.; White, E. K.; Pan, J. T.-C.; Knight, S. A. B.; Morgenstern, A. R.; Bianco, C.; Planet, P. J.; Gardner, S. E.; Grice, E. A. Variable Staphyloxanthin Production by Staphylococcus aureus Drives Strain-Dependent Effects on Diabetic Wound-Healing Outcomes. *Cell Rep.* **2023**, *42*, 113281.
(50) Daniella, I.; Diego, C.; Marco, M.; Maximiliano, F.; Vinicius, C. Neutrophil Function Impairment Is a Host Susceptibility Factor to Bacterial Infection in Diabetes. In *Cells of the Immune System*, Ota, F.; Seyyed Shamsadin, A., Eds.; IntechOpen, 2019, p 2.
(51) Sawant, K. V.; Sepuru, K. M.; Lowry, E.; Penaranda, B.; Frevert, C. W.; Garofalo, R. P.; Rajarathnam, K. Neutrophil Recruitment by Chemokines Cxcl1/Kc and Cxcl2/Mip2: Role of Cxcr2 Activation and Glycosaminoglycan Interactions. *J. Leukoc. Biol.* **2021**, *109*, 777−791.

https://doi.org/10.1021/acsnano.4c14057
ACS Nano 2025, 19, 11807−11822

(52) Deng, J.; Jiang, R.; Meng, E.; Wu, H. Cxcl5: A Coachman to Drive Cancer Progression. *Front. Oncol.* **2022**, *12*, 944494.
(53) Ridiandries, A.; Tan, J. T. M.; Bursill, C. A. The Role of Chemokines in Wound Healing. *Int. J. Mol. Sci.* **2018**, *19*, 3217.
(54) Bongers, S.; Hellebrekers, P.; Leenen, L. P. H.; Koenderman, L.; Hietbrink, F. Intracellular Penetration and Effects of Antibiotics on Staphylococcus aureus inside Human Neutrophils: A Comprehensive Review. *Antibiotics* **2019**, *8*, 54.
(55) Ye, W.; Zhao, H.; Dai, Y.; Wang, Y.; Lo, Y. H.; Jan, L. Y.; Lee, C. H. Activation and closed-state inactivation mechanisms of the human voltage-gated KV4 channel complexes. *Mol. Cell* **2022**, *82*, 2427−2442.e4.
(56) Feske, S.; Wulff, H.; Skolnik, E. Y. Ion Channels in Innate and Adaptive Immunity. *Annu. Rev. Immunol.* **2015**, *33*, 291−353.
(57) Grimes, D.; Johnson, R.; Pashos, M.; Cummings, C.; Kang, C.; Sampedro, G. R.; Tycksen, E.; McBride, H. J.; Sah, R.; Lowell, C. A.; Clemens, R. A. Orai1 and Orai2Modulate Murine Neutrophil Calcium Signaling, Cellular Activation, and Host Defense. *Proc. Natl. Acad. Sci.* **2020**, *117*, 24403−24414.
(58) Shin, E. H.; Li, Y.; Kumar, U.; Sureka, H. V.; Zhang, X.; Payne, C. K. Membrane Potential Mediates the Cellular Binding of Nanoparticles. *Nanoscale* **2013**, *5*, 5879−5886.
(59) Perez-Figueroa, E.; Alvarez-Carrasco, P.; Ortega, E.; Maldonado-Bernal, C. Neutrophils: Many Ways to Die. *Front. Immunol.* **2021**, *12*, 631821.
(60) Rosch, J. W.; Sublett, J.; Gao, G.; Wang, Y. D.; Tuomanen, E. I. Calcium Efflux Is Essential for Bacterial Survival in the Eukaryotic Host. *Mol. Microbiol.* **2008**, *70*, 435−444.
(61) Truman, L. A.; Ford, C. A.; Pasikowska, M.; Pound, J. D.; Wilkinson, S. J.; Dumitriu, I. E.; Melville, L.; Melrose, L. A.; Ogden, C. A.; Nibbs, R.; Graham, G.; Combadiere, C.; Gregory, C. D. Cx3cl1/Fractalkine Is Released from Apoptotic Lymphocytes to Stimulate Macrophage Chemotaxis. *Blood* **2008**, *112*, 5026−5036.
(62) Torr, E. E.; Gardner, D. H.; Thomas, L.; Goodall, D. M.; Bielemeier, A.; Willetts, R.; Griffiths, H. R.; Marshall, L. J.; Devitt, A. Apoptotic Cell-Derived Icam-3 Promotes Both Macrophage Chemoattraction to and Tethering of Apoptotic Cells. *Cell Death Differ.* **2012**, *19*, 671−679.
(63) Elliott, M. R.; Chekeni, F. B.; Trampont, P. C.; Lazarowski, E. R.; Kadl, A.; Walk, S. F.; Park, D.; Woodson, R. I.; Ostankovich, M.; Sharma, P.; Lysiak, J. J.; Harden, T. K.; Leitinger, N.; Ravichandran, K. S. Nucleotides Released by Apoptotic Cells Act as a Find-Me Signal to Promote Phagocytic Clearance. *Nature* **2009**, *461*, 282−286.
(64) Morioka, S.; Maueroder, C.; Ravichandran, K. S. Living on the Edge: Efferocytosis at the Interface of Homeostasis and Pathology. *Immunity* **2019**, *50*, 1149−1162.
(65) Kourtzelis, I.; Hajishengallis, G.; Chavakis, T. Phagocytosis of Apoptotic Cells in Resolution of Inflammation. *Front. Immunol.* **2020**, *11*, 553.
(66) Doran, A. C.; Yurdagul, A., Jr.; Tabas, I. Efferocytosis in Health and Disease. *Nat. Rev. Immunol.* **2020**, *20*, 254−267.
(67) Yousefi, S.; Stojkov, D.; Germic, N.; Simon, D.; Wang, X.; Benarafa, C.; Simon, H. U. Untangling "Netosis" from Nets. *Eur. J. Immunol.* **2019**, *49*, 221−227.
(68) Yipp, B. G.; Petri, B.; Salina, D.; Jenne, C. N.; Scott, B. N.; Zbytnuik, L. D.; Pittman, K.; Asaduzzaman, M.; Wu, K.; Meijndert, H. C.; Malawista, S. E.; de Boisfleury Chevance, A.; Zhang, K.; Conly, J.; Kubes, P. Infection-Induced Netosis Is a Dynamic Process Involving Neutrophil Multitasking in Vivo. *Nat. Med.* **2012**, *18*, 1386−1393.
(69) Tarai, B.; Das, P.; Kumar, D. Recurrent Challenges for Clinicians: Emergence of Methicillin-Resistant Staphylococcus aureus, Vancomycin Resistance, and Current Treatment Options. *J. Lab. Physicians* **2013**, *5*, 71−78.
(70) Gardete, S.; Tomasz, A. Mechanisms of Vancomycin Resistance in Staphylococcus aureus. *J. Clin. Invest.* **2014**, *124*, 2836−2840.
(71) Wei, J.; Qiao, S.; Zhang, X.; Li, Y.; Zhang, Y.; Wei, S.; Shi, J.; Lai, H. Graphene-Reinforced Titanium Enhances Soft Tissue Seal. *Front. Bioeng. Biotechnol.* **2021**, *9*, 665305.

https://doi.org/10.1021/acsnano.4c14057
ACS Nano 2025, 19, 11807−11822